Appendix Simulation Studies of Direct Photon Production at STAR

August 25, 1998

A.1 Introduction

This appendix gives a more detailed description of the simulation methods and results presented in the endcap electromagnetic calorimeter (EEMC) proposal. The main focus of these studies has been to gain an increased understanding of the $\vec{p}\vec{p} \to \gamma + \text{jet} + X$ reaction, intended to be studied at the RHIC collider using the STAR detector. Measurement of inclusive direct photon production will also be performed using the PHENIX detector. When polarized proton beams are accelerated at RHIC, it will be possible to study direct photon production over the range of collision energies, $50 \leq \sqrt{s} \leq 500$ GeV. The emphasis in this study is on two collision energies: $\sqrt{s} = 200$ and 500 GeV. The principal components of the STAR detector relevant to measurements of $\gamma +$ jet coincidences are the time-projection chamber (TPC), the silicon vertex tracker (SVT), the barrel electromagnetic calorimeter (BEMC) and the proposed endcap electromagnetic calorimeter (EEMC).

The primary physics objective of the STAR-spin experimental program is the determination of the *polarized gluon* structure function of the proton, $\Delta G(x)$, referring to the probability difference of finding gluons longitudinally polarized parallel versus antiparallel to the proton's polarization. There are similar polarized structure functions for the valence and sea quarks in the proton. The ratio of polarized to unpolarized *quark* structure functions is well measured from a series of recent polarized deep inelastic lepton scattering (DIS) experiments at SLAC and CERN [2,3]. All polarized structure functions depend on the fraction of the proton's momentum carried by the specific parton, the so-called Bjorken x variable. A major objective in this simulation study is the examination of systematic errors in the determination of the polarized gluon structure function for the proton as a function of the gluon momentum fraction x_g.

Direct photon production at large perpendicular momentum transfer (p_T) in high-energy *pp* collisions with longitudinally polarized proton beams is an attractive method for determining $\Delta G(x)$ because the reaction is dominated by the quark-gluon Compton scattering process, $qg \to \gamma q$, that is well described in leading-order perturbative QCD [7]. This process is known to have a large partonic spin correlation coefficient, $\hat{a}_{LL}$, particularly when the photon is detected in the direction of the incident quark [11]. The scattering angle, ϑ^*, of the photon in the partonic center of mass (pCM) is measured relative to the direction of the incident gluon. For *qg* Compton scattering the spin correlation coefficient monotonically increases from $\hat{a}_{LL} = 0$ at $\cos\vartheta^* = +1$, to $\hat{a}_{LL} = +1$ at $\cos\vartheta^* = -1$, the latter meaning that when the photon is detected in the direction of the incident quark, the scattering occurs only when the helicities of the quark and gluon are of like sign. As well, in leading-order (LO) pQCD, the cross section angular distribution for gluon Compton scattering has a pole at $\cos\vartheta^* = -1$. Hence, by emphasizing partonic kinematics where the quark polarization is known to be large from deep-inelastic lepton scattering experiments ($x_q \geq 0.2$) and $\cos\vartheta^*$ approaches -1, the polarized quark serves as an extremely efficient *analyzer* of the gluon polarization. An additional constraint is imposed to minimize the contributions of higher-twist processes. We will require that the transverse momentum of the photon be greater than 10 GeV/c.

One goal of experiments aimed at determining $\Delta G(x)$ is to establish the zeroth moment of this distribution:

$$\Delta G = \int_0^1 \Delta G(x)dx. \qquad \text{(A.1)}$$

Loosely speaking, ΔG represents the fraction of the proton spin carried by gluons. It is expected that $\Delta G(x)$ will have important contributions to the integral from small x. The implication for *pp* scattering is that the apparatus should be capable of probing asymmetric partonic collisions — $x_g \leq 0.1$ and $x_q \geq 0.2$ — meaning that the pCM has a large velocity in the *pp* collider reference frame,

$$\beta_{pCM} = \frac{x_q - x_g}{x_q + x_g}, \qquad \text{(A.2)}$$

and the final state reaction products are boosted in the direction of the incident quark when $x_q > x_g$. This is the fundamental motivation for appending an EEMC to the STAR detector for these measurements. It also introduces a severe experimental difficulty; namely, by simultaneously demanding $p_T \geq 10$ GeV/c and highly asymmetric partonic collisions, the detected photon is necessarily highly energetic, since $E_\gamma = p_T \cosh\eta_\gamma$, expressed in terms of the photon pseudorapidity, η_γ. Experimentally, this presents a challenge of how to distinguish between a single energetic photon at the EEMC versus two closely spaced energetic photons arising from the decay of a neutral meson, such as a π^0 or an η^0. For those particles, the minimum opening angle between the two decay photons ($\phi_{\gamma\gamma}^{\min} = 2\sin^{-1}(m/E)$) is also the most probable value for the decay. High p_T mesons (direct mesons) are leading particles in jets, formed by the hadronization of quarks or gluons. Even though the fragmentation probability is small for a single meson to carry a substantial fraction of the momentum of a recoiling quark or gluon, the cross sections for partonic processes such as *qg* or *gg* elastic scattering that contribute to the direct meson yield are much larger than those that produce direct photons. This results in the expectation that the direct meson yield will be larger than the direct photon yield.

Despite several previous descriptions of direct photon production experiments with STAR [46], there remain many open questions, some of which will be addressed in this writeup. The principal questions include

- to what extent can other event information for the direct meson background be used to distinguish them from direct photons?
- what is the expected spin dependence of the direct meson background events?
- what is the optimal design for the endcap detector to distinguish between isolated direct photons and mesons? How can information from the endcap detector be used for this distinction?
- how well can the kinematics of the partonic collisions be determined for individual events from measured quantities for γ + jet coincidences?
- to what extent can the polarized gluon structure function be *directly extracted* from measured asymmetries for the $\vec{p}\vec{p} \rightarrow \gamma + \text{jet} + X$ reaction? What are the systematic errors in this determination?

Various assumptions have been made in this study. Ultimately, these assumptions must be checked carefully in further simulation studies. The initial assumptions are

1) The expected TPC pileup that will be present for high luminosity *pp* running (**L** = $0.4\sqrt{s}$ $(\mu\text{b}\cdot\text{s}\cdot\text{GeV})^{-1}$ can be fully eliminated by the event reconstruction software. An earlier study of this problem has been presented in Ref. [43]. Further studies

are most certainly necessary. We will assume below that TPC pileup can be rejected completely, and that no charged particle tracking information from the direct photon events of interest is lost by the pileup rejection algorithm.

2) It is assumed for simplicity that the charged particle tracking is 100% efficient and that the momentum resolution for charged particles can be expressed as

$$\frac{\delta p_T}{p_T} = a + bp_T\,, \qquad \text{(A.3)}$$

where a and b are independent of the scattering angle, or equivalently the pseudorapidity (η). The values $a = 1.1\%$ and $b = 0.24\ \%\cdot(\mathrm{GeV}/c)^{-1}$ have been used in these studies to simulate the TPC resolution at mid-rapidity ($|\eta| < 1$). This is consistent [56] with previous simulation studies of the TPC, restricted to the mid-rapidity region, where the TPC readout is maximally sensitive to the track. For $1 < |\eta| < 2$, only a portion of the TPC readout is sensitive to the track, and the p_T resolution is expected to worsen substantially, especially as $|\eta| \rightarrow 2$. More complete simulation studies are required to establish the η dependence of the p_T resolution for charged particles. For now, it is assumed that the errors in p_T are distributed according to a Gaussian distribution with sigma equal to δp_T, given by Eqn. A.3. Furthermore, it is also assumed that the interaction point and the track direction at the interaction point can be determined with errors small compared to other reconstruction errors discussed below.

3) It is assumed that a suitable event trigger [41] can be designed, permitting a high efficiency selection of direct photon + jet coincidence events, but with manageable rates in the STAR data acquisition system for background events at the luminosity needed for the measurements.

Recently, we have begun to address some of these starting assumptions. Regarding the ability to trigger on jets, it is likely that correlating electromagnetic energy measurements from the barrel and endcap EMC with charged particle multiplicity measurements obtained from the central trigger barrel (CTB) and multi-wire chambers (MWC) from the TPC pad readout will greatly enhance the efficiency of a jet trigger. More detailed studies of suitable jet triggers are underway. Studies of the performance of the TPC for charged particle tracking at large pseudorapidity ($1 < |\eta| < 2$) are also underway. Even though the loss in momentum resolution at large η has only a minimal impact on direct photon measurements, a discussion of the preliminary investigations is included here (Sec. A.2.4) for completeness.

A.2 Description of the Simulation Program

A.2.1 PYTHIA

The starting point for the simulation studies is PYTHIA [42] (version 5.7), operated primarily in its default mode. For selected events, specified below, features of the PYTHIA event record are mapped onto a HBOOK n-tuple. The final-state particles that fall within either the TPC or E(B)EMC acceptance are considered to be observable and are analyzed to establish either if they are within the *isolation cone* around a candidate direct photon or if they can be reconstructed as a *jet*.

All of the PYTHIA calculations reported below were done with a cut on the partonic transverse momentum, $\hat{p}_T$, requiring a minimum value of 10 GeV/c. Selection of direct photon events in PYTHIA is possible via an input parameter, thereby allowing only $q(\bar{q})g \to q(\bar{q})\gamma$, $q\bar{q} \to \gamma g$ or $q\bar{q} \to \gamma\gamma$ processes to be generated. For $\sqrt{s}$ = 200 GeV *pp* collisions and the limitation that $\hat{p}_T > 10$ GeV/c, the cross sections within PYTHIA used to select the relative proportion of events from these three processes are respectively 3.0, 0.55 and 2.6×10^{-3} nb. A lower $\hat{p}_T$ threshold results in much larger values for these process dependent cross sections, and consequently, longer processing time to generate the same integrated luminosity.

The direct meson background events are significantly more difficult to simulate. They are simulated by using the default settings for *pp* scattering within PYTHIA, including all possible 2 → 2 partonic hard scattering processes. Requiring a minimum of 10 GeV/c transverse momentum for the partonic hard scattering, the yield of high p_T neutral mesons (π^0 and η^0) that fall within the STAR acceptance and subsequently decay primarily into pairs of photons (or other sizable decay modes for the η^0) is determined by searching through the hadronic debris for the largest p_T π^0 or η^0 meson that is within the acceptance of STAR. The event is accepted if the $\pi^0(\eta^0)$ has $p_T \geq 10$ GeV/c. For $\sqrt{s}$ = 200 GeV *pp* collisions and the limitation that $\hat{p}_T > 10$ GeV/c, the sum of all such processes within PYTHIA yields a total cross section of 6.4 μb, dominated by gluon elastic scattering (σ = 2.2 μb) and $q(\bar{q})g \to q(\bar{q})g$ (σ = 3.2 μb). When a *direct meson* event is found, the event is treated as a candidate direct photon event and is stored in the n-tuple and the analysis proceeds.

The advantage of performing simulations of this sort is that the 'right answer is known.' So, in addition to storing the final state particle information into the n-tuple, the variables describing the partonic hard-scattering (particle identities, kinematic definition, etc.) are stored to facilitate the determination of the accuracy of the event reconstructions.

Additional information stored in the n-tuple allows application of various isolation cuts (discussed in detail below) to help distinguish between direct photons and $\pi^0(\eta^0)$ mesons. Kinematic information is stored for up to twenty observable particles $P \equiv \gamma, \pi^{\pm}, K^{\pm}, p^{\pm}$ (p^+ refers to protons and p^- to antiprotons; the observable particle definition excludes all neutral long-lived hadrons, for which the response of the EMC is quite small) that fall within a cone of 'radius'

$$R \equiv \sqrt{\left(\eta_P - \eta\right)^2 + \left(\phi_P - \phi\right)^2} < 0.7, \qquad \text{(A.4)}$$

where (ϕ,η) refer to the azimuthal angle and pseudorapidity of the direct photon candidate (either γ, π^0 or η^0) and (ϕ_P,η_P) refers to the direction of the observable particle at its origin. By storing the kinematic information for all particles within a broad isolation cone around the direct photon candidate it is possible to perform studies of the influence of different isolation algorithms without having to regenerate the event samples. The results presented here are for a much more restrictive isolation condition, described in Sec. A.3.1.

Finally, all observable particles, excluding the direct photon candidate (assuming that it can be easily distinguished from the other particles in the event by its characteristically large energy deposition in the EMC), are passed to a 'jet finder', based on an algorithm developed for UA1 and subsequently modified for use in STAR [45]. To keep the size of the HBOOK n-tuple to manageable proportions, only the *results* of the jet finder are saved. Details about the performance of the jet finder are presented in Sec. A.4.1.

The simulations done to this point include both initial-state (IS) and final-state (FS) radiation, as modeled by the default settings of PYTHIA. Physically, this corresponds to including both gluon radiation and gluon splitting ($g \to q\bar{q}$) processes by the initial state partons. One effect of IS radiation is to introduce transverse momentum components to the initial state partons, qualitatively described as k_T-smearing effects, which are larger in magnitude than those associated with the confinement size of the proton. The magnitude of k_T-smearing introduced by IS radiation has been a controversial topic. Some authors [8] claim the need for more k_T-smearing, beyond that included in next-to-leading-order (NLO) pQCD calculations, to provide a consistent determination of the *unpolarized* gluon structure function extracted from cross section measurements of inclusive direct photon production in high-energy $p\bar{p}$ collisions at different values of $\sqrt{s}$. They have found that the IS radiation model employed by PYTHIA provides the necessary smearing [8]. Another effect of IS radiation is to substantially alter the Bjorken x value of the parton before the hard scattering, particularly for gluons. The kinematic reconstructions made possible by the coincident detection of the direct photon and the recoiling jet at STAR, described in detail in Sec. A.4.2, determine the Bjorken x values of the partons involved in the hard scattering; *i.e.*, *after* IS radiation. In most cases, the accuracy of the kinematic reconstructions are dominated by k_T smearing effects rather than by finite measurement resolution. Finally, it is possible for the partonic hard scattering to occur from one of the IS radiation products. For example, a gluon Compton scattering event could be initiated by a gluon arising from IS radiation from a u quark. Modifying the procedure used to predict polarization observables (described in Sec. A.2.2) to account for the effects of IS radiation probably requires a full NLO pQCD treatment, which is beyond the scope of the present study.

OPEN QUESTIONS

1) To what extent do default PYTHIA settings properly model (*a*) the direct photon yield?; (*b*) the direct meson yield?; and (*c*) jet properties and jet yields?
2) How large is the contribution of high p_T photons produced from parton fragmentation? Is this background sufficiently suppressed with isolation cuts?

A.2.2 Inclusion of Polarization Observables

PYTHIA does not include polarization observables for *pp* scattering. Polarization effects are added after the PYTHIA event generation using separate polarized and unpolarized structure functions and the partonic-process-dependent LO pQCD results for $\hat{a}_{LL}$. All of the calculations presented here are based on the Gehrmann-Stirling (GS) set A fits [6] to polarized DIS measurements. As is evident in Table I, the LO pQCD expressions for $\hat{a}_{LL}$ depend on the ratio of the partonic Mandelstam variables, $\hat{s}, \hat{t}$ and $\hat{u}$. That dependence reduces in all cases to a power series in cos ϑ^*, the cosine of the pCM scattering angle. The spin correlation coefficient for a *pp* scattering event is computed as

$$A_{LL} \sim P_1 P_2 \hat{a}_{LL} = \frac{\Delta f_1(x_1, Q^2)}{f_1(x_1, Q^2)} \frac{\Delta f_2(x_2, Q^2)}{f_2(x_2, Q^2)} \hat{a}_{LL}(\hat{s}, \hat{t}, \hat{u}), \qquad \text{(A.5)}$$

assuming the incident protons have 100% polarization. The parton polarizations (P) are then given as the ratio of the polarized (Δf) to unpolarized (f) parton distribution functions for either quarks or gluons depending on the partonic identities and the Bjorken x values given by PYTHIA for the initial state hard scattering, following initial-state radiation. For u and d quarks

$$
\begin{aligned}
q(x,Q^2) &= q_{valence}(x,Q^2) + q_{sea}(x,Q^2) \\
\Delta q(x,Q^2) &= \Delta q_{valence}(x,Q^2) + \Delta q_{sea}(x,Q^2)\ .
\end{aligned}
\tag{A.6}
$$

For antiquarks and strange quarks or strange antiquarks, only the sea-quark distribution functions are used. In the GS fits [6], the same sea quark polarized structure functions is used for both sea quarks and sear antiquarks, independent of their flavor. For gluons, model polarized distribution functions, consistent with scaling violations in polarized DIS measurements, are employed. It is important to keep in mind that the existing DIS measurements provide only very loose constraints on $\Delta G(x)$. The partonic hard-scattering kinematics from PYTHIA, following initial-state radiation, are used to determine the momentum fraction, x, and ‘scale’ (Q^2) for the structure functions. The partonic-process dependent value for $\hat{a}_{LL}$ is computed using the Mandelstam variables for the hard scattering given by PYTHIA. Expressions for $\hat{a}_{LL}$ for different partonic processes [11] are given in Table I and are graphically displayed as a function of ϑ^* in Fig. A.1. From the expressions, it is clear that in the pCM, $\hat{a}_{LL}$ can be reduced to a power series in cos ϑ^*. The dependence on the partonic x arises only through the motion of the pCM in the laboratory frame. Similar expressions exist for the differential cross section. Of particular interest to the study of the gluon polarization via the qg Compton process, is a pole in the LO pQCD expression for the cross section at $\vartheta^* = \pi$, precisely where $\hat{a}_{LL}$ reaches its maximal value.

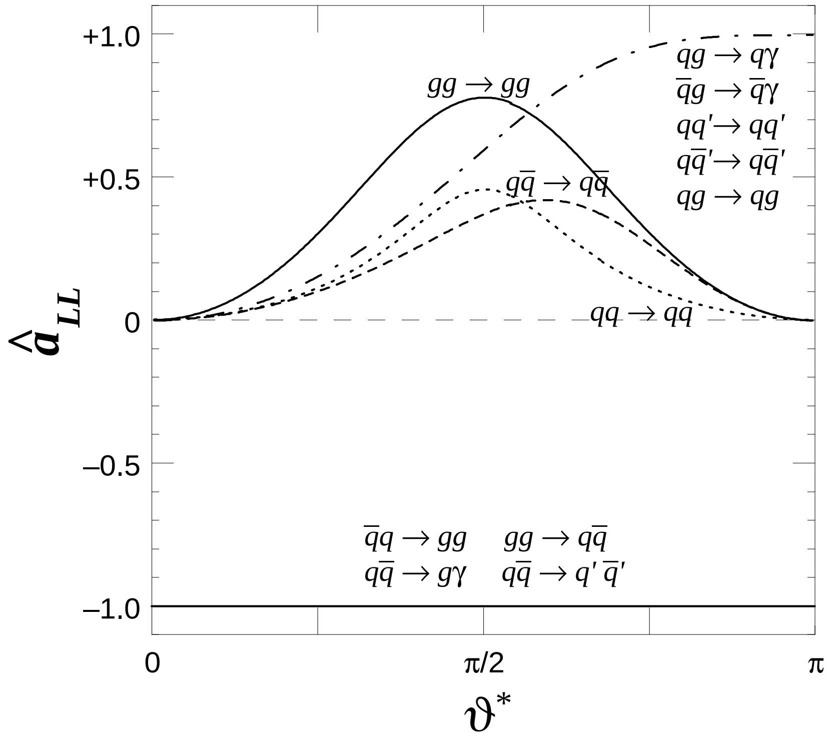

Figure A.1 Leading-order pQCD predictions for the variation of the spin-longitudinal spin correlation versus the pCM scattering angle for different 2 → 2 partonic subprocesses. The notation qq' refers to unlike quark flavors in the initial (final) state.

We can anticipate the following, based on the LO pQCD predictions for the process-dependent $\hat{a}_{LL}(\cos\vartheta^*)$

- the 10% contribution of the $q\bar{q} \rightarrow g\gamma$ process to the direct-photon yield will dilute the measured A_{LL} for collisions between longitudinally polarized proton beams since $\hat{a}_{LL} = -1$ for this process at all ϑ^*.
- the expectation is that direct meson production will have a non-zero A_{LL} since the "x_q" > 0.2 condition we impose on analyzed events will suppress *gg* scattering contributions, and the next most dominant process will be *qg* scattering. Since *qg* elastic scattering has an identical $\hat{a}_{LL}$ to gluon Compton scattering, we might expect A_{LL} for direct meson production could be quite similar to that from direct photon production, if the direct meson arises primarily from quark, rather than gluon, fragmentation. This will only be true for ϑ^* near $\pi/2$. At other angles, $\cos\vartheta^*$ will be positive for direct mesons produced by quark fragmentation whereas it is negative for direct photon production, meaning that A_{LL} should be smaller for the background process. Some differences will also arise because of the contribution of *qq* elastic scattering.

Table I Partonic-process dependent spin-correlation coefficients.

Process	$\hat{a}_{LL}$
$qq \rightarrow qq$	$\frac{(\hat{s}^2-\hat{u}^2)/\hat{t}^2+(\hat{s}^2-\hat{t}^2)/\hat{u}^2-\frac{2}{3}\hat{s}^2/\hat{t}\hat{u}}{(\hat{s}^2+\hat{u}^2)/\hat{t}^2+(\hat{s}^2+\hat{t}^2)/\hat{u}^2-\frac{2}{3}\hat{s}^2/\hat{t}\hat{u}}$
$q\bar{q}' \rightarrow q\bar{q}'$ $qq' \rightarrow qq'$ $qg \rightarrow qg$	$\frac{(\hat{s}^2-\hat{u}^2)}{(\hat{s}^2+\hat{u}^2)}$
$q\bar{q} \rightarrow q'\bar{q}'$ $q\bar{q} \rightarrow gg$ $gg \rightarrow q\bar{q}$	-1
$q\bar{q} \rightarrow q\bar{q}$	$\frac{(\hat{s}^2-\hat{u}^2)/\hat{t}^2-(\hat{u}^2+\hat{t}^2)/\hat{u}^2+\frac{2}{3}\hat{u}^2/\hat{t}\hat{s}}{(\hat{s}^2+\hat{u}^2)/\hat{t}^2+(\hat{u}^2+\hat{t}^2)/\hat{s}^2-\frac{2}{3}\hat{u}^2/\hat{t}\hat{s}}$
$gg \rightarrow gg$	$\frac{-3+2\hat{s}^2/\hat{u}\hat{t}+\hat{u}\hat{t}/\hat{s}^2}{3-\hat{s}\hat{u}/\hat{t}^2-\hat{s}\hat{t}/\hat{u}^2-\hat{u}\hat{t}/\hat{s}^2}$
$qg \rightarrow \gamma q$	$\frac{(\hat{s}^2-\hat{u}^2)}{(\hat{s}^2+\hat{u}^2)}$
$q\bar{q} \rightarrow \gamma q$	-1

There are several additional assumptions implicit to this method of appending polarization observables to events generated by PYTHIA. One is that partonic polarizations are unaffected by initial-state radiation. Another is that there are no polarization effects in the fragmentation of the final-state partons to the observed hadrons that depend on initial-state polarizations. The first of these assumptions can only be relaxed with a next-to-leading order pQCD calculation.

One difficulty that remains in these simulations is the treatment of evolution. In general, the parton distribution functions employed for these calculations are determined at small Q^2, typically ~4 GeV^2, by fits [6] to DIS measurements. Although the appropriate scale to use for *pp* scattering remains controversial, it is generally assumed that $Q^2 \propto p_T^2$. For the calculations done here, $Q^2 = \frac{1}{2} p_T^2$. With this assignment, high-p_T direct photon production at STAR will typically probe values of Q^2 of ~100 GeV^2, meaning that the polarized parton structure functions must be evolved to this much higher scale. This is properly done using the Altarelli-Parisi equations with polarized splitting functions [57]. To this point, only an approximate treatment of evolution, originally employed by Bourrely, Soffer, Renard and Taxil for their analysis of polarization effects in high-energy colliders, has been used. The polarized and unpolarized parton distribution functions used to incorporate polarization effects into PYTHIA are shown in Fig. A.2 at two different scales, using the approximate treatment of evolution from Ref. [11].

Most recently, we have applied a numerical solution to the QCD evolution equations from Ref. [57] to the fitted polarized structure functions of Ref. [6]. The results for the Bjorken x dependence of the polarized structure functions, evolved to the higher Q^2 values probed in proton collisions at RHIC, were then fitted to a general functional form (Eqn. A.20) typically used to analyze DIS results. The resulting expansion coefficients from Eqn. A.20 are then parameterized as functions of Q^2 over the interval $20 \leq Q^2 \leq 200$ GeV^2. The shape of $x\Delta G(x)$ from this proper treatment of evolution compares quite favorably to what is displayed in Fig. A.2a. There are some differences for the other polarized structure functions, particularly those for the sea quarks. The simulations of the polarization observables for direct photon + jet coincidences using these structure functions are underway.

The simplest manner to combine A_{LL} values for different events in a Monte Carlo simulation is to ‘determine’ the state of the beam polarizations for the event. This determination is made via a statistical method, based on the probability of the occurrence of an event in a given beam crossing which is distributed according to a Poisson distribution. In these studies only two beam polarization states were considered. It is possible to consider more, particularly when sources of *false asymmetries* are included into the simulation. Here, the "+" state corresponds to both beams having positive helicities and the "–" state is when one of the two beams has positive and the other negative helicity. The beam polarizations used in these studies are $P_{b_1} = P_{b_2} = 0.7$. The average yield of events ($\mu_\pm$) per bunch crossing will then vary with the polarization state as

$$\mu_\pm = (1 \pm P_{b_1} P_{b_2} A_{LL}) N_{eff}, \qquad \text{(A.7)}$$

where A_{LL} is computed for the event from Eqn. A.5 and the polarization is assumed to have the same magnitude for the colliding beams. In this equation, N_{eff} represents the average number of interactions for each unpolarized bunch crossing. The real value for this variable is quite small. So instead of the true value, a much larger effective value is used to limit the needed CPU time; physically, this corresponds to a larger value of the luminosity.

The polarization state to associate with the event generated by PYTHIA is chosen at random using the following procedure. For a single polarization state, a random value, N_{int}, is drawn from a Poisson distribution whose mean is $\mu_+(\mu_-)$. The random variable represents the number of interactions for this particular ‘bunch crossing’ or trial random variable. If $N_{int} > 0$, it is assumed that the event generated by PYTHIA corresponds to the +(–) polarization state depending on whether $\mu_+(\mu_-)$ is used. The sign is alternated in Eqn. A.7 until some interaction occurs.

The effectiveness of this method for determining the beam polarization state for the event is illustrated in Fig. A.3. Here, we consider N_{trial} independent simulations of an asymmetry

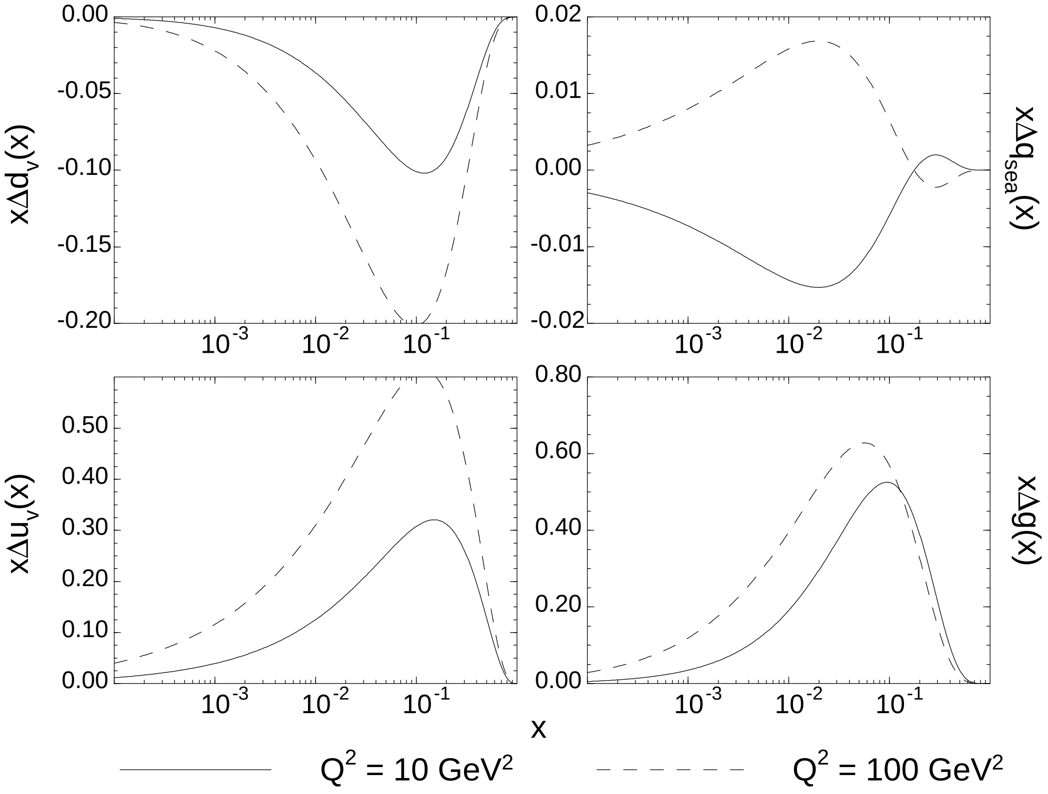

Figure A.2a Polarized parton distribution functions at two different scales. The values at small Q^2 are similar to those in [6].

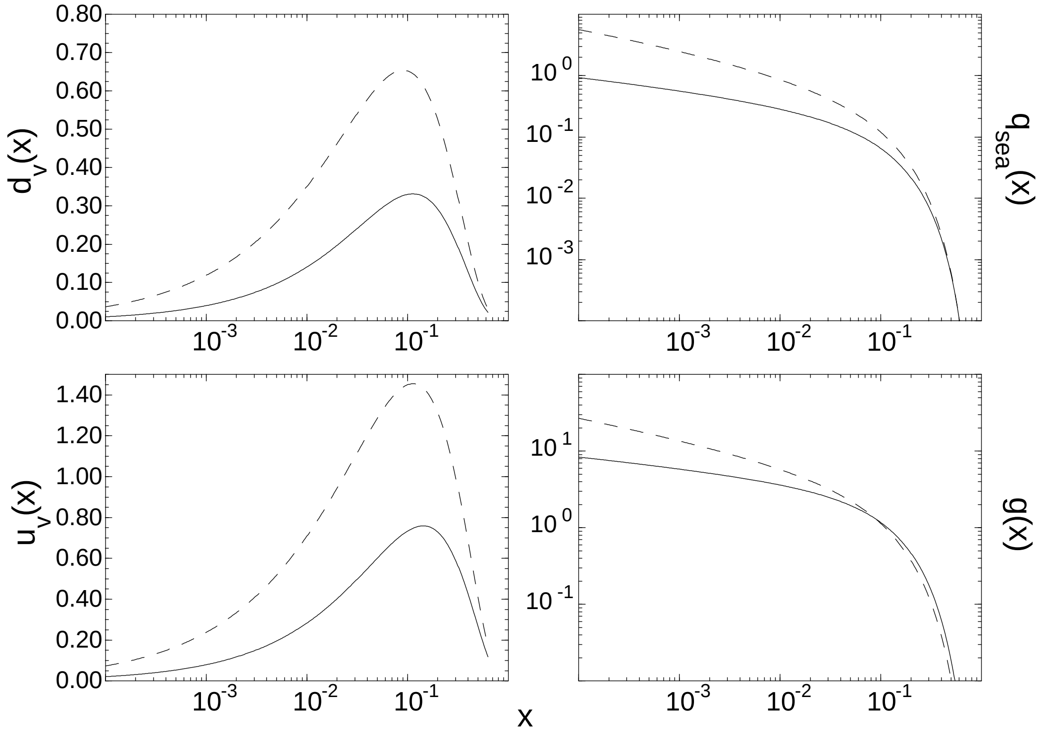

Figure A.2b Unpolarized parton distribution functions at two different scales. The values at small Q^2 are similar to those in [6].

measurement, where for each measurement, there are N_{total} events generated in each trial which are assigned to one of two beam spin states following the above procedure, using beam polarizations

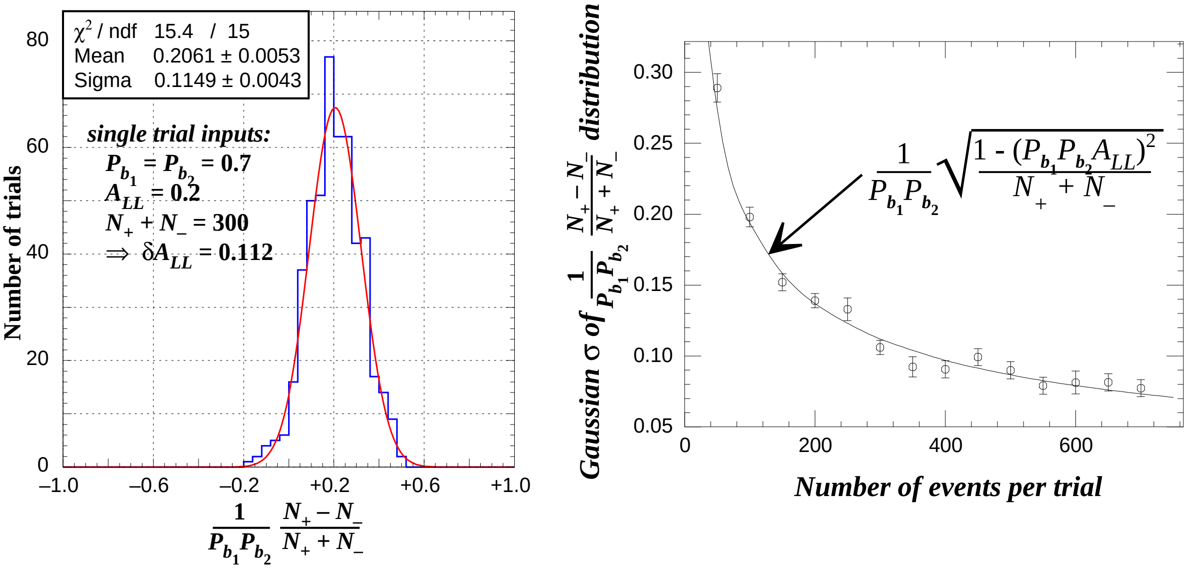

Figure A.3 (Left) Distribution of results for the A_{LL} polarization observable obtained from analyzing 500 different trials. For each trial, the beam polarization is statistically deduced event-by-event as described in the text. (Right) Dependence of the Gaussian sigma, deduced from analysis of the distribution polarization observables for multiple trials, on the number of events ($N_+ + N_-$) per trial.

$P_{b_1} = P_{b_2} = 0.7$. The input A_{LL} is 0.2 and the beam polarization state is statistically determined using $N_{eff} = 0.01$. If the procedure is valid, then the reconstructed value of A_{LL} from a single trial, determined from the number of generated counts in each spin state ($N_\pm$):

$$A_{LL}^{recon} = \frac{1}{P_{b_1}P_{b_2}} \frac{N_+ - N_-}{N_+ + N_-}, \qquad \text{(A.8)}$$

should be distributed according to a Gaussian distribution for the N_{trial} independent simulations. The sigma of the Gaussian distribution of reconstructed A_{LL} values should be equal to the estimated error from a single trial, or

$$\delta A_{LL} = \frac{1}{P_{b_1}P_{b_2}} \sqrt{\frac{1 - (P_{b_1}P_{b_2}A_{LL})^2}{N_+ + N_-}}. \qquad \text{(A.9)}$$

As is evident from Fig. A.3, the method of deducing the beam polarization on an event-by-event basis leads to the expected statistical precision for the spin asymmetry estimated from the $N_+ + N_-$ events from a single trial. Similarly studies have been conducted with a range of values of N_{eff} yielding comparable results.

OPEN QUESTIONS

1) What effect does a proper, rather than the approximate, treatment of the Q^2 evolution of the structure functions have on the predictions for A_{LL}?
2) Is the assumption that initial-state radiation has no effect on spin-dependent structure functions valid?

A.2.3 GEANT Studies of a Model Calorimeter

In principle, the PYTHIA event generator output can be input to a full simulation of the response of the STAR detector, including the proposed EEMC addition. Ultimately, this step must be taken to get a full understanding of the requirements of the direct photon measurements. As a step in that direction, the response of a 'pseudodetector' to only direct photons or direct mesons has been studied, with the objective of quantitatively establishing the degree to which they can be separated.

The 'pseudodetector' is an alternating stack of antimonial-lead (90% Pb - 10% Sb, thickness 5 mm) and plastic scintillator sheets (thickness 4 mm). After each pair of sheets, there is a 3-mm air gap assumed to allow routing of fiber readout of the scintillator. There are 25 layers of identical construction, save for the shower-maximum detector (SMD) described below. [NOTE: as discussed below, this stack is slightly deeper than the 23-layer calorimeter described in the proposal. The response of the proposed calorimeter is approximated by summing the energy loss from the first 23 layers.] The longitudinal geometry of the stack is similar to that described in reference [38]. In the transverse direction, the stack is divided into 9 towers, arranged into a 3×3 matrix. The transverse dimensions of each tower are 14 cm × 14 cm, corresponding to an acceptance of $\Delta\eta = \Delta\phi = 0.1$ at $\eta \sim 1.5$ when the perpendicular distance to the front face of the pseudodetector is positioned at 273 cm from the interaction point. After the fifth set of sheets, two plastic scintillator SMD planes, each having 4-mm total thickness, are positioned. The SMD is constructed from long scintillator strips oriented with their long axes parallel to the layer structure of the pseudodetector; the two planes are rotated by 90° with respect to each other. The strips have a triangular cross section, and resemble a position-sensitive preshower detector developed for the D0 upgrade [34]. For the simulations, the triangular base of the scintillator strips is 1 cm long and is also parallel to the layer structure of the EMC. The base-to-apex distance is 4 mm; a schematic diagram is shown in Fig. 9. Excluding details of the SMD structure, the pseudodetector for which the modeling was conducted was based on one of the earlier designs considered for the EEMC mechanical structure. Subsequently, this design has evolved to improve its mechanical stability at the expense of reducing the total number of radiation lengths compared to Ref. [38], although, many other essential features of the calorimeter, including the number of radiation lengths per layer, the thickness of the scintillator sampling layer and the inclusion of a shower-maximum detector (SMD) after the fifth layer, are basically unchanged.

For the calculations presented here, photons and neutral mesons are always normally incident on the 'pseudodetector.' The distance of the detector relative to the interaction point is adjusted for each event to account for the variation of the pathlength to the EMC module with η, based on the actual geometry of the STAR detector. Also possible is to adjust both the distance and the angle of incidence. Calculations of this sort are underway.

Electromagnetic showers are simulated through this model EEMC, including the SMD, using GEANT. The energy loss from electrons and positrons within the shower are recorded for each event when they are incident on either the scintillator sheets or the SMD planes. Separate recording of the energy loss through each of the 9 tower members in one EEMC layer and in each SMD strip is performed. The tower summed energy loss is computed for the first 23 of the 25 layers, reflecting the present mechanical design of the EEMC. From the ratio of the centroid of the 23-layer tower sum to the E_0 parameter obtained from the gamma distribution fit to the longitudinal profile (see Fig. A.4), it can be concluded that 98% of the average shower produced by a normally incident 30 GeV photon is contained within the detector. This level of containment limits non-linearities in the EEMC response for high-energy electrons and photons. The sampled energy loss is 6.6% of the incident photon energy over a broad range of photon (and electron or positron) energies. Event fluctuations in the showers lead to a spread in energy deposition, $\sigma/\Delta E$ = 3.4 % at 30 GeV.

Following a procedure used by others, the transverse shower profile as measured by the SMD *u* and *v* planes is fitted by the sum of three common-centroid Gaussians with independent widths and scaling. The narrowest Gaussian has a sigma of ~0.5 strips and the sigma of the second Gaussian is ~3.1 times greater. As seen in Fig. A.4, this gives a reasonable description of the simulated shower's transverse profile. Better descriptions of the average transverse profile are available, but are not suitable for the analysis of the SMD profile from single events. This results

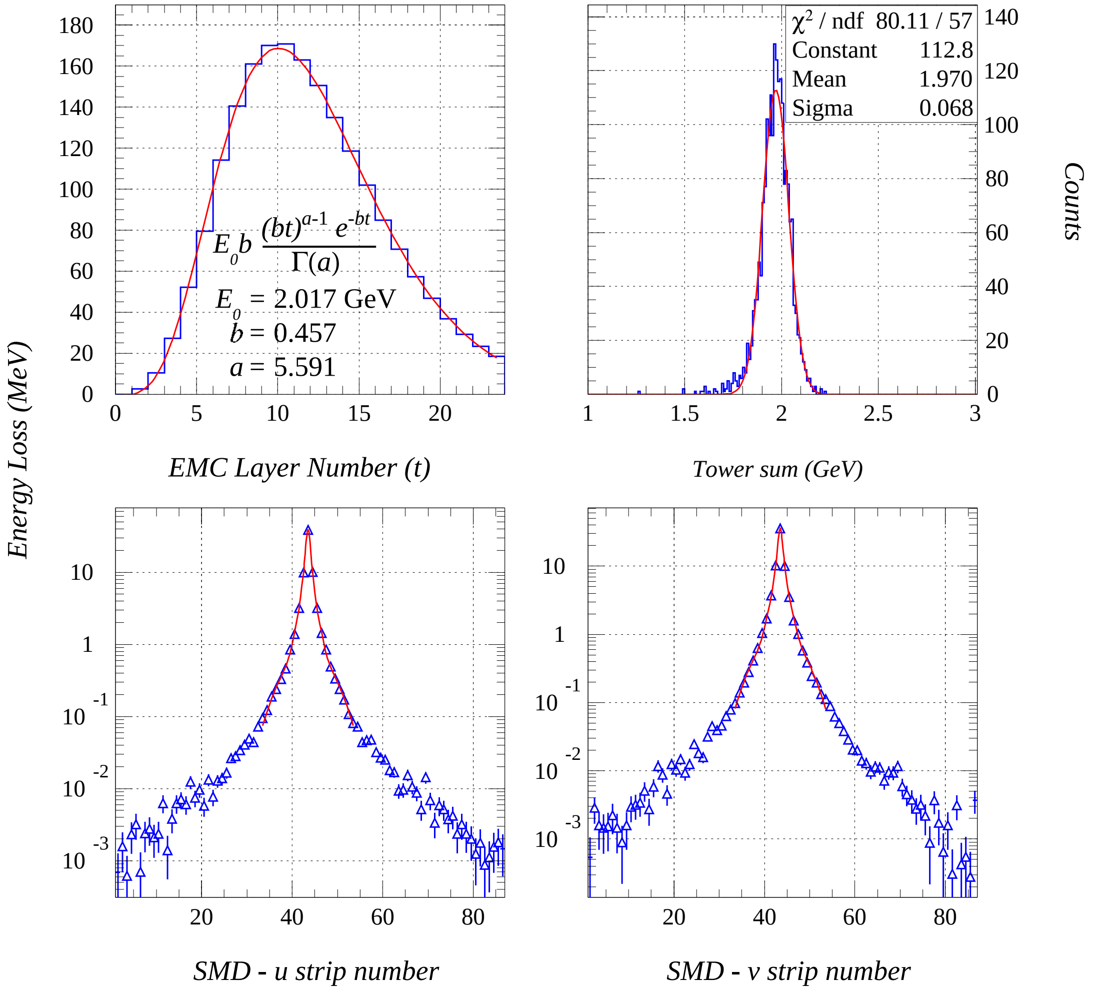

Figure A.4 Response of the pseudodetector to monoenergetic 30-GeV photons, normally incident at the center of the detector, as simulated by GEANT. The distributions represent averaged (summed) quantities for 2,000 events. (Upper left) Average energy loss in MeV within each 4-mm thick scintillator layer of the pseudodetector. The longitudinal profile is well fit by a gamma distribution, with the parameters shown. (Upper right) The event distribution of the 23-layer tower summed energy loss (in GeV). The distribution is fit by a Gaussian. (Bottom row) Average energy loss in MeV through the SMD *u*,*v* planes. These distributions have been fit as described in the text.

because the extended tails of the average SMD profile are not uniformly populated for individual events. Instead, they arise from the small probability for large-angle bremsstrahlung, producing an energetic photon or electron at relatively large angles with respect to the direction of the primary radiation, thereby producing small secondary peaks which can be significantly displaced from the primary energy deposition in the individual-event SMD profile. The secondary peak structure is lost when examining the average SMD profile since, for different events, their separation from the primary energy loss peak varies. The average energy deposited in the u(v) plane, integrated over all strips, is 74 (72) MeV for a normally incident 30 GeV photon. The v plane sees less energy loss, and the transverse profile is correspondingly broader, because the u plane in front of it absorbs the low energy electron component of the shower and introduces significant multiple scattering. The average energy deposition in the u(v) plane increases linearly with $\sqrt{E_\gamma}$ consistent with the statistical variation in the number of secondaries; for a normally incident 90 GeV photon, the average energy deposited in the u plane for is 144 MeV.

Returning to the calorimeter proper, the summed energy loss in an active element is then converted into an ADC response by assuming on average two detected photoelectrons (*pe*) per minimum ionizing particle (MIP) traversing 4 mm of scintillator. The simulated energy loss for the element is converted into a mean number of photoelectrons, μ_{pe}, by scaling it by the most probable energy loss as computed by GEANT for a MIP normally incident on a 4-mm thick plastic scintillator (ΔE_{MIP} = 642 keV) and the assumed 2 *pe* / MIP. That value is then used to choose a random number of observed *pe* for the detector element from a Poisson distribution with mean μ_{pe}. The ADC response is then given by the sum of Gaussian random numbers chosen independently for each *pe* from a distribution that reflects the response of a photomultiplier to a single *pe*. The PMT gain is chosen to realistically represent the dynamic range required of the EEMC. The low end of the range is determined by the requirement of being able to see a MIP penetrating the 23-layer stack. This corresponds to a mean energy deposition of 14.8 MeV, equivalent to an incident 220 MeV photon, assuming an energy-independent sampling fraction of 6.6% for showers induced by photons. The high end of the range is set by the requirement of detecting high-energy electrons from W decay. The electron p_T spectrum has a peak at 40 GeV/c

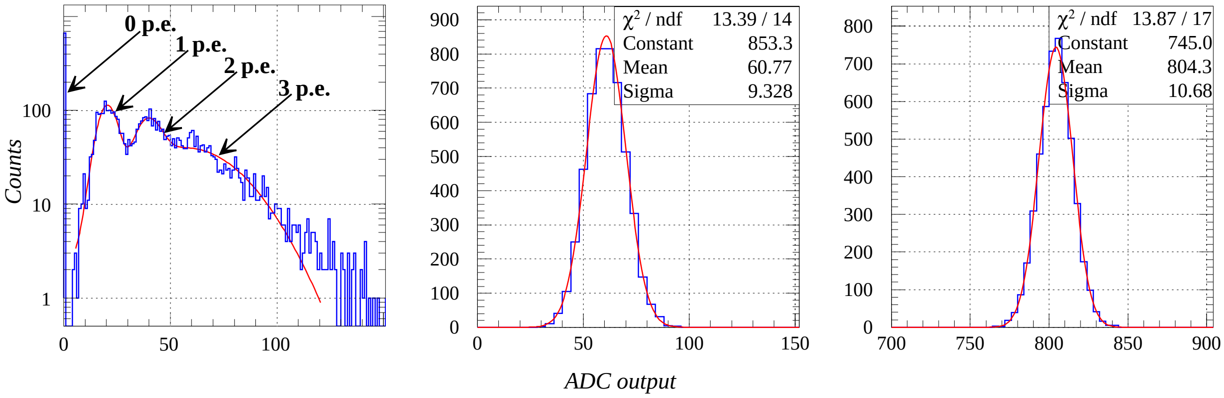

Figure A.5 Simulated ADC output, following a procedure described in the text. (Left) the simulated response of a PMT reading out a MIP normally incident on a 4-mm thick scintillator with μ_{pe} = 2. The PMT gain is set higher than for the other two figures. (Middle) the ADC output for a MIP normally incident on a 23-layer stack with the PMT gain set a factor of 10 higher than for γ detection. (Right) the ADC output for an ‘average’ 30 GeV photon, with the energy-loss per layer given by the average response predicted by GEANT (Fig. A.4).

and drops rapidly to zero for larger values (Fig. 17). At the $\eta = 2$ EEMC acceptance limit, this corresponds to a 150 GeV electron. Allowing for finite resolution, this requires a dynamic range in excess of 1000:1, implying the use of at least an 11-bit ADC. It is assumed here that a 12-bit will be employed; the gains are adjusted accordingly in Fig. A.5 showing the ADC output for a MIP normally incident on a 23-layer stack and for a 30-GeV photon. To illustrate the influence of the photostatistics on the EEMC resolution, the energy loss from each layer corresponds to the average values as shown in Fig. A.4. Even at only 2 *pe* / MIP for the light output from the scintillator layers of the EMC, the resolution of the EEMC is still dominated by shower-to-shower fluctuations rather than by photostatistics.

In contrast to the requirements of the light output from the EEMC scintillator layers, the light output from the triangular cross section scintillating strips for the SMD is crucially important. In particular, the performance of the SMD for $\gamma / \pi^0(\eta^0)$ separation will critically depend on this. The development of extruded scintillator strips with axial wave-length-shifting (WLS) fiber light collection from the scintillator has been carried out by the D0 collaboration [34]. Their scheme for collecting scintillation light uses visible-light photon counters (VLPC), which have a substantially greater quantum efficiency at the peak of the emission spectrum from the WLS than do multi-anode photomultiplier tubes (MAPMT) envisioned for use for the EEMC SMD. Recently, the D0 collaboration has tested such a detector built from triangular cross section strips with dimensions, 6.5 mm (base width) × 6 mm (apex-to-base height), in high-energy beams of pions and electrons [58]. Their preliminary result is 11 ± 2 detected *pe* / MIP. Scaling this result to the detector thickness proposed for the EEMC SMD, and accounting for the difference in quantum efficiencies of VLPC and MAPMT, we assume that it is possible to detect 2 *pe* / MIP. This number is used for the simulation results presented in Sec. A.3.2.

OPEN QUESTIONS

1) What is the optimum depth of the SMD within the EEMC for $\pi^0(\eta^0) / \gamma$ separation over the spectrum of energies expected for direct photon production in the energy range $200 \leq \sqrt{s} \leq 500$ GeV?
2) What is the mean number of detected photoelectrons from a MAPMT for a MIP traversing the full thickness of the triangular cross section scintillator with the light collected by WLS fibers, as proposed for use in the EEMC SMD? Will cross talk in the MAPMT limit the performance of the SMD?

A.2.4 Simulation studies of the TPC response

We are only at a very early stage in the necessary assessment of the TPC performance for the physics program envisioned for the endcap EMC addition to the STAR detector. The initial focus of the simulation studies has been to establish quantitatively the accuracy of the extraction of ΔG, including reasonable assumptions about the resolution and acceptance of the various STAR detectors. Most recently, we have begun examining some of these assumptions in more detail. One outstanding question is the expected momentum resolution of the TPC in tracking charged particles at large $|\eta|$. A longer term problem will be to revisit the question of how best to reject the substantial pileup in the TPC expected for enhanced luminosity *pp* runs, required to achieve the desired statistical errors on the measurements.

The first approach to establish how the resolution of the TPC varies with η is based on an estimate [59] for the accuracy of the inverse radius variable ($k = 1/R$, where the radius of curvature of the charged particle track in a uniform magnetic field of strength B is $R \propto p_T/B$). At large p_T, and correspondingly large curvature radius, multiple scattering has only small effects, and δk can be approximated by

$$\delta k \approx \frac{\varepsilon}{L'^2}\sqrt{\frac{320}{N+4}}, \qquad \text{(A.10)}$$

when N uniformly spaced measurements, each of spatial accuracy ε, are made along the *observed* track length projection, L', on the bend plane. The factor of 320 in Eqn. A.10 is appropriate when the reaction vertex is included in the fit to the charged particle track. The uncertainty δk gives rise to a linear dependence of the relative momentum resolution with p_T; the factor b in Eqn. D.3. Eqn. A.10 suggests that there are two effects on the relative p_T resolution in the interval, $1 \leq |\eta| \leq 2$:

- the relative p_T resolution worsens in inverse proportion to the square of the *observed track length projection*, which is shortening as $|\eta|$ goes beyond unity for the TPC.
- the relative p_T resolution also worsens in inverse proportion to the square root of the number of TPC pad rows involved in the measurement. The decreased pad row density for the inner sector (at large $|\eta|$) causes a dramatic loss in resolution beyond $|\eta| \approx 1.5$.

These effects are even larger when accounting for the further reduction in the observed track length projection caused by the time to generate the level-0 trigger and switch open the TPC gating grid.

It is important to note that little is demanded from TPC measurements at large $|\eta|$ for the direct photon + jet coincidence measurements that we propose to use for the determination of the contribution of gluons to the spin of the proton. For direct photon measurements, the TPC is required to establish that an *isolated* neutral particle is responsible for the large energy deposition in the endcap EMC (the isolation criteria are discussed in Sec. A.3.1). The charged particle component of jets will result from TPC measurements; but, the crucial *jet direction*, necessary to reconstruct the partonic kinematics (Sec. A.4.1), depends very little on the momentum resolution. Where the TPC resolution matters most is for the detection of high-p_T electrons and positrons ($e^{\pm}$) from $W^{\pm}$ decay, as discussed in Sec. 3.5. For those measurements, the decreased p_T resolution will affect the ability to discriminate $e^{\pm}$ from hadrons. Secondly, the ability of the TPC to distinguish between the oppositely signed curvature for electrons and positrons with large p_T (≥ 35 GeV/c) is impaired.

The general trends for the relative momentum resolution of the TPC as suggested by Eqn. A.10 have been confirmed in a simple simulation. In that simulation, the helical path followed by a charged particle in the (assumed uniform) solenoidal magnetic field of STAR is traced outward from a vertex at the center of the detector. Space points are saved when the projection of the helix on to the bend plane crosses the pad rows of the TPC. These space points are then blurred by random values, drawn from a Gaussian distribution with $\sigma_x = \sigma_y = \sigma_z = 0.1$ cm. The primary vertex is blurred in a similar manner. The charged particle trajectory is followed to the SMD of the endcap EMC, since it will provide a reliable space point, particularly for high-p_T electrons and positrons from $W^{\pm}$ decay. The assumed resolution of this point is 0.25 cm (σ), consistent with the results from the analysis of the SMD data (Sec. A.3.2). The resulting points (primary vertex, plus TPC and SMD space points) are then fit by the MOMENTM routine from the CERN library [60].

The distribution of *k* values obtained from fits to a large number of charged particle events characterized by fixed η and p_T is found to be Gaussian, with a sigma similar to that found from Eqn. A.10. At high p_T, the reconstructed p_T distribution is skewed, with the most probable value being systematically too large. This arises because tracking a charged particle through a magnetic field establishes *k* rather than p_T. One conclusion from this preliminary study is that the TPC tracking resolution deteriorates sufficiently rapidly beyond $|\eta| \approx 1.5$ to the point of limiting its ability to distinguish the sign of the particle's charge based on the track curvature for $p_T \geq 35$ GeV/c, values probed in $W^{\pm}$ production. It is possible that some of this ability can be recovered by imposing a constraint on the track fit to agree with much higher resolution measurement of E_T made by the EMC.

More detailed simulation studies of the TPC performance using the physics analysis modules within STAF are underway. After verifying the TPC performance at large $|\eta|$, studies of the rejection of TPC pileup expected for enhanced luminosity *pp* running will be pursued.

A.3 Direct Photon Yields and Background Processes

Probably the most difficult and the most important aspect of the measurement is the distinction between direct photons and direct mesons. Fig. A.6 shows the η distribution of photon (signal) and meson (background) events subject to the condition $10 \leq p_T \leq 20\ \mathrm{GeV/c}$, and no other cuts, for $\sqrt{s} = 200$ GeV proton collisions, as generated by PYTHIA. The background:signal ratio is 13:1; considering only π^0 events, the ratio reduces to 8:1. This is somewhat higher than earlier attempts to deduce this ratio from data [46]. Those previous attempts involved substantial extrapolation of measurements (with differing definitions of direct meson yields) at different p_T, η and $\sqrt{s}$ to arrive at the estimates. It is considered here that the PYTHIA results are in reasonable enough agreement with the extrapolated data to provide a useful estimate of the background. More importantly, the use of PYTHIA will enable an assessment of the effectiveness of various other aspects of the events to suppress the background.

The p_T dependence of the background:signal ratio varies rapidly above 10 GeV/c. The origin of this dependence is that high p_T $\pi^0(\eta^0)$ mesons originate predominantly as fragments of recoiling partons, carrying only a small fraction of the parton's transverse momentum, governed by the appropriate fragmentation functions. Hence, the low p_T portion of the direct meson spectrum is populated from high p_T final-state partons which are themselves distributed according to an exponentially falling spectrum. The simulated γ spectrum has only small contributions from fragmentation and has an exponential falloff with p_T that more closely matches that of the partons, rather than the parton fragmentation products. As a result, the background:signal ratio falls steeply with p_T.

Still, the quality of the direct photon measurements at STAR will be determined by how well this large background can be reduced. Event-by-event distinctions are most desirable to limit the loss of statistical precision (and the introduction of systematic error) for the $\Delta G(x)$ determination. There are two possible sources of background reduction that fall into this category

- examination of the response of the remainder of the STAR detector to see if the candidate direct photon event is *isolated.*
- analysis of the data from the shower maximum detector.

For events that satisfy each of the above cuts there still is a background to the direct photon yield that can be measured and subtracted. Statistical subtractions of the remaining background are available from

- analysis of data from a preshower detector
- identified direct meson events

Detail about how direct meson events are identified are presented in Sec. A.3.2. At present, the details about how a preshower detector could be used to distinguish between direct photon and direct meson events have not been worked out. Qualitative arguments about the benefit of a preshower detector for $\gamma / \pi^0(\eta^0)$ separation have been presented in Ref. [61].

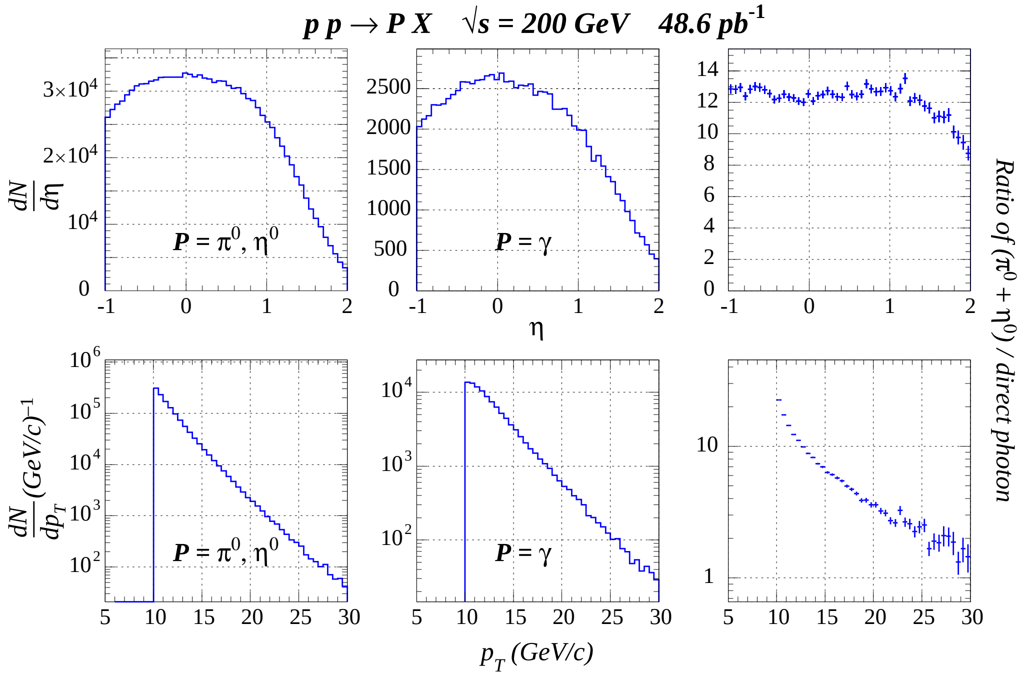

Figure A.6 Direct meson (π^0,η^0) and direct photon yields from PYTHIA versus pseudorapidity (top) and versus p_T (bottom) for pp collisions at $\sqrt{s}$ = 200 GeV. The rightmost column of the figure shows the ratio. The only condition applied to the η distribution is $10 \leq p_T \leq 20$ GeV/c and to the p_T distribution is $-1 \leq \eta \leq 2$.

Neutral meson backgrounds for $\sqrt{s}$ = 500 GeV proton collisions have also been examined. The general trends observed in Fig. A.6 are quite similar to what is observed at this higher energy. The effectiveness of the SMD for distinguishing the neutral meson background from the direct photon signal is expected to depend only on p_T, meaning that measurements at the two collision energies will face similar backgrounds, when considering a fixed p_T range.

A.3.1 Isolation Cuts

Isolation cuts have been used in all previous experimental studies of direct photon production. Their impact on the interpretability of the measurements is controversial, with some authors claiming that the failure to obtain consistent unpolarized gluon structure functions from direct photon production cross sections measured in pp or $p\bar{p}$ collisions can be traced to the isolation cuts used to analyze the data. This should not be as important a concern for measurements of polarization observables at STAR since they depend on the ratio of the difference to the sum of yields from different beam spin states (Eqn. A.18). So long as the relevant fragmentation functions carry no memory of the initial-state polarizations, overall normalization factors, that are relevant for cross section measurements, cancel out for polarization observables.

In brief, the ‘distance’ between a photon (detected by the E/BEMC) or charged particle (detected by the TPC) observed at (η,ϕ) and a candidate direct photon event observed at $(\eta_\gamma,\phi_\gamma)$ is defined as

$$R=\sqrt{(\eta_\gamma-\eta)^2+(\phi_\gamma-\phi)^2}\,. \qquad \text{(A.11)}$$

Only photons, with energies greater than 0.3 GeV, and charged particles, with transverse momentum greater than 0.3 GeV/c, that are within the acceptance of STAR are considered detectable. The actual lower limit on photon energy and charged particle p_T that can be included in the isolation condition must be determined by a complete simulation including effects of TPC pileup and may be substantially larger. The candidate direct photon is said to be isolated if no other detectable photon or charged particle falls within a cone of ‘radius’ $R \le R_{\max}$. It is assumed that the detection efficiency for neutrons, anti-neutrons and K_L^0 mesons is zero. Fig. A.7 shows the summed energy spectra and particle multiplicity for the choice of $R_{\max}=0.26$, employed by UA2 in their analysis [47] of direct photon data.

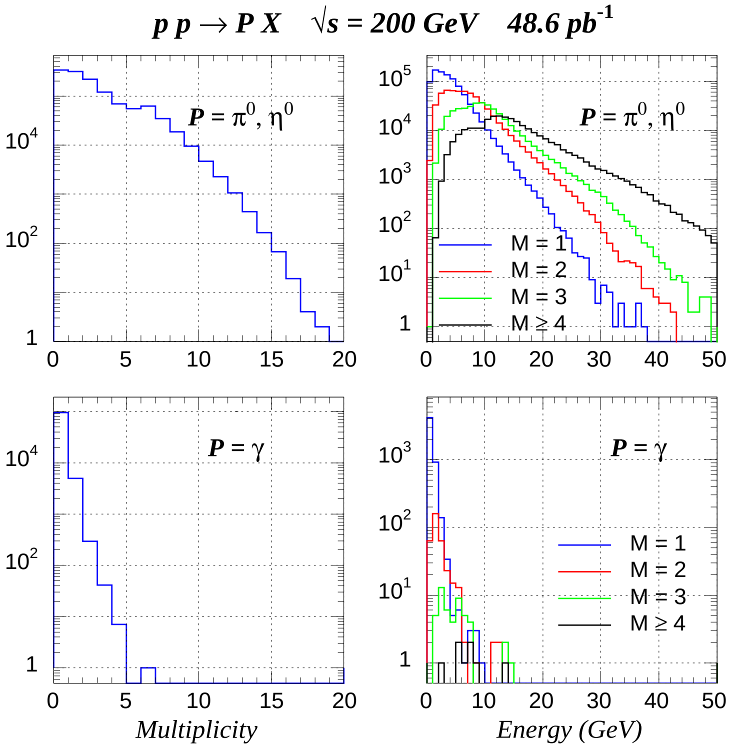

Figure A.7 The multiplicity and summed energy distributions of particles falling within an isolation cone of radius R = 0.26 around a direct meson (top) or direct photon (bottom) candidate.

With the restrictive definition used by UA2, there is a suppression of 77% of the background direct mesons and a loss of 13% of the signal. The η and p_T distributions of *isolated* direct mesons and photons are shown in Fig. A.8 with the isolation cuts imposed, the other cuts identical to that used for Fig. A.6. Following the application of the UA2 isolation cut, the background:signal ratio is 3:1, with the direct π^0 component being 2:1. The η dependence of the ratio of the *isolated* direct meson yield to *isolated* direct photon yield shows the influence of the finite detector acceptance; near the edges of the detector, the isolation cuts are less effective. One advantage of the UA2 isolation cut is the relative insensitivity of the direct meson suppression on p_T. Other choices — for example, defining an isolation condition on the fractional difference in total energy contained within cones of different radii around the direct photon candidate — may not share this feature.

The η^0 meson contribution to the background is expected to be better suppressed by the shower maximum detector information since the minimum photon opening angle is larger and the two-photon branching ratio is only 38%. Further background suppression by isolation cuts is possible to consider by examining the total energy within a cone of radius, R, rather than by demanding no particles within that cone. From Fig. A.7, it is clear that the particles falling within the isolation cone around the direct photon are substantially softer than those for the direct meson. Hence, a more sophisticated condition for isolation, based on the total energy observed in the isolation cone for different multiplicities, could allow the use of a large radius cone, thereby further reducing the direct meson background without substantial loss of the direct photon signal.

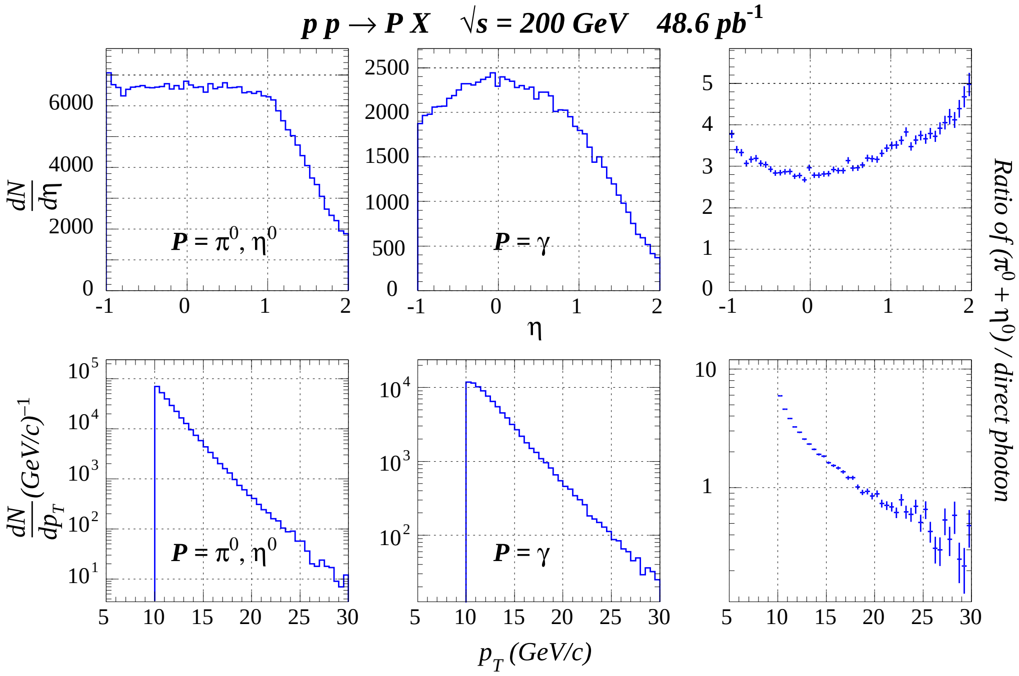

Figure A.8 *Isolated* direct meson (π^0,η^0) and direct photon yields from PYTHIA versus pseudorapidity (top) and versus p_T (bottom) for *pp* collisions at $\sqrt{s}$ = 200 GeV. The rightmost column of the figure shows the ratio. In addition to the conditions described in the caption to Fig. A.6, it is required that there are no additional detectable particles in a cone of radius, R=0.26, around the direct meson and direct photon.

OPEN QUESTIONS

1) Will a more sophisticated isolation cut provide the same p_T - independent suppression of the π^0(η^0) background as the UA2 condition? How much more of the background can be suppressed?
2) How will isolation cuts be affected by TPC pileup and the poor EMC response to hadrons?

A.3.2 Analysis of Shower Maximum Data

The basic idea of a shower maximum detector is to obtain a good measurement of the transverse extent of an electromagnetic shower to distinguish between events where a single photon compared to a pair of closely spaced photons (produced in the decay of a neutral meson) are incident on the detector. One method of making this distinction is to perform a moment analysis of the SMD response [62]. As has been shown previously, algorithms based on moment analyses of SMD data for a single event work well below $E \sim 10$ GeV, but are not as effective above ~20 GeV, because of the smaller spatial separation between the two photons from $\pi^0(\eta^0)$ decay and because of shower-to-shower fluctuations of the transverse profile for different events.

An alternative method for analyzing the SMD data is to attempt *peak fits* to establish whether one, or more than one, photon initiates the electromagnetic shower. The procedure followed here to analyze the GEANT simulations was to attempt a *single peak fit* to the SMD data. The general form of the lineshape used was the sum of two common-centroid Gaussians, similar, but not identical, to the lineshape used to describe the average response of the SMD to showers initiated by a beam of monoenergetic photons or electrons normally incident on the detector (described in Sec. A.2.3). This lineshape is simpler than that used to describe the *average*

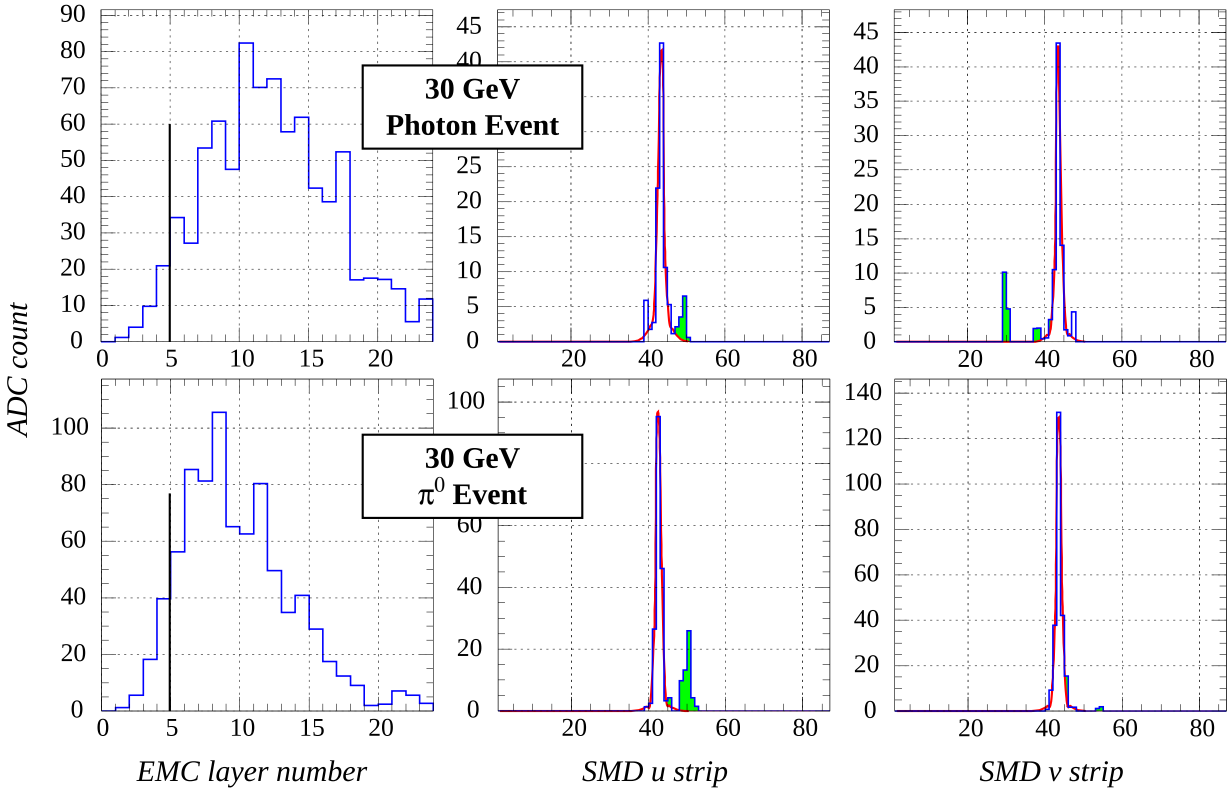

Figure A.9 Simulated ADC output from the 23-layer EMC and the SMD u,v planes for a normally incident 30 GeV photon (top) and a 30 GeV π^0 (bottom). The vertical line in the plots on the left indicate the position of the SMD. The π^0 decays into a 26.5 and 3.5 GeV photon. The plane of the decay is perpendicular to the SMD u strips and the opening angle between the two photons is ~14 mr. The γ event has a small secondary peak due to bremsstrahlung. The fitted lineshape in each case is similar to that found for the average SMD response to a single photon, but with parameters adjusted to best fit the data for the single generated event. The shaded portion of the SMD response is the 'sided' fit residual, defined in the text.

transverse profile of the electromagnetic shower, because the statistical precision of the measurement in a *single event* is limited. These limitations arise because of event-to-event variations in the point where the incident photon first converts into a e^+e^- pair, statistical fluctuations in the number of secondaries produced and the expected small light output of individual SMD detector elements for a single MIP incident on the detector. These statistical fluctuations not only require a simpler lineshape to describe the transverse profile of the primary energy deposition but can also lead to additional structures within the profile for a shower initiated by a *single photon*. The non-Gaussian tails of the average SMD response are manifested in a single event as isolated depositions of energy, spatially separated from the primary shower. These additional peaks, when significant, can mimic the SMD response to di-photon interactions, as seen in Fig. A.9.

Ideally, it would be possible to search for either a single or a di-photon interaction by fitting either one or two peaks to the single-event SMD data and choosing the fit that has the smallest reduced χ^2. Single peaks in both SMD planes would then be associated with single photon interactions and two peaks in either or both of the SMD planes would be associated with di-photon interactions. An analysis of this type, using MINUIT for the multi-parameter optimization, was tried, and subsequently abandoned because of problems with numerical stability. Because of these problems, an alternate algorithm was developed that had significantly fewer numerical problems. This method relied on a single peak fit to the SMD event data followed by a 'sided' moment analysis of the 'fit residual' distribution defined as

$$\begin{aligned} \mu_t - 40 < t < \mu_t - 2\sigma_t &\Rightarrow R_-(t) = D(t) - F(t) \\ \mu_t + 40 > t > \mu_t + 2\sigma_t &\Rightarrow R_+(t) = D(t) - F(t)\ . \end{aligned} \qquad \text{(A.12)}$$

where t refers to either of the two transverse coordinates measured by the SMD (u,v); μ and σ are the centroid and 'narrow' Gaussian sigma from the single peak fit; $D(t)$ refers to the data; $F(t)$ refers to the lineshape of the fitting function; and $R_\pm(t)$ is the residual distribution. The maximum zeroth moment from each SMD plane, $R_{0,t} = \max\{R_{0+,t}, R_{0-,t}\}$, is then found and is used to discriminate between direct γ events and direct $\pi^0(\eta^0)$ events. The integration range used to determine $R_{0\pm}$ is important to consider. The range must be large enough to distinguish between single and di-photon events that are within the same EMC tower. Extending the range too far could result in too high an average occupancy in the SMD patch involved in the discrimination, causing loss of direct photon events.

Figure A.10 shows the discrimination between single and di-photons via the correlation between the zeroth moment of the SMD response summed over the u and v planes ($R_{0,u} + R_{0,v}$) and the integrated energy loss in the largest SMD peak, summed over the u and v planes. The events populating this histogram were generated by PYTHIA for the $pp \rightarrow \gamma + jet + X$ and $pp \rightarrow \pi^0(\eta^0) + jet + X$ reactions at $\sqrt{s}$ =200 GeV. Only those photons or neutral mesons that satisfied all of the cuts (defined in Eqn. A.16) were used to have GEANT generate showers in the pseudodetector. To account for the η dependence of the pathlength to the EMC detectors as they will be configured within STAR, the interaction point was shifted relative to the position of the pseudodetector. This procedure approximately accounts for the η-dependence of the spatial separation of the two photons from neutral meson decay at the detector. In these simulations, the photons and neutral mesons were chosen to be normally incident on the detector. An alternative method is to account for the angle of incidence on the detector, based on the actual geometry of the barrel and endcap. Calculations of this sort are underway.

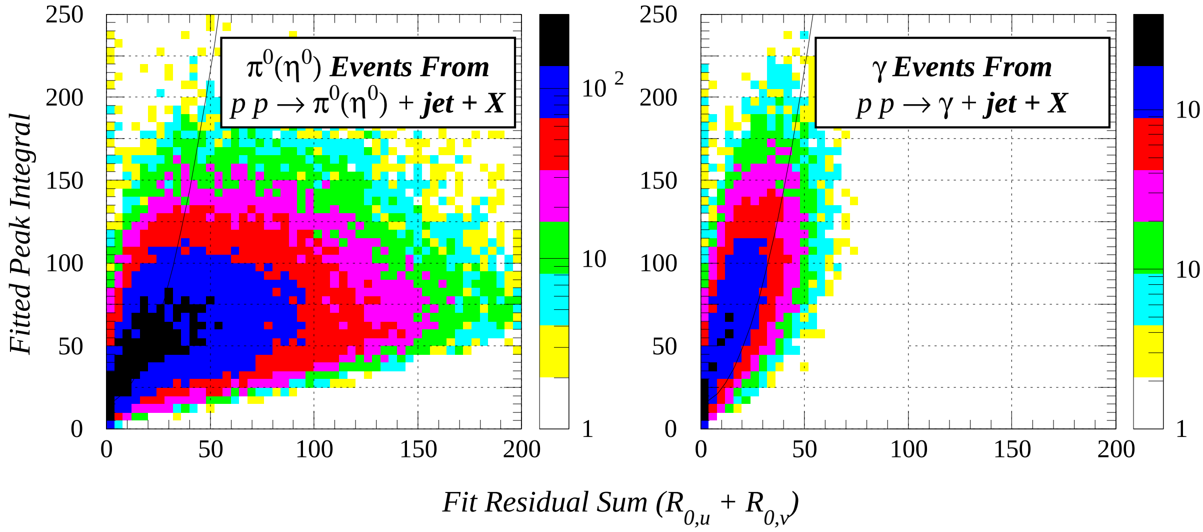

Figure A.10 The individual event SMD data is analyzed to distinguish between γ and $\pi^0(\eta^0)$ following an algorithm specified in the text. The line is used as a cut to identify $\pi^0(\eta^0)$. Events are generated for the two reactions with an integrated luminosity of 43 pb^{-1}. Only events that satisfy all kinematic cuts (specified in Sec. A.4.2) are considered here.

Details of the suppression of $\pi^0(\eta^0)$ from the SMD cut displayed in Fig. A.10 are presented in Secs. 3.3 (see especially Fig. 15). One comment here is about $\pi^0(\eta^0)$ events *that pass all cuts consistent with a direct photon*, including the SMD cut. Fig. A.11 shows the distribution of relative energy sharing between the two photons arising from $\pi^0(\eta^0)$ decay for events that pass the SMD photon identification. The distribution is peaked at the energy sharing variable, $z_\gamma = \pm1$, corresponding to maximal asymmetry in the energies of the two photons. The smooth background near $|z_\gamma| \sim 0$ corresponds to fluctuations in the depth at which one of the two photons first converts into an e^+e^- pair. The result is that the *fake direct photons* from $\pi^0(\eta^0)$ decay most closely resemble *real direct photons*, since one photon from the meson decay is of low energy.

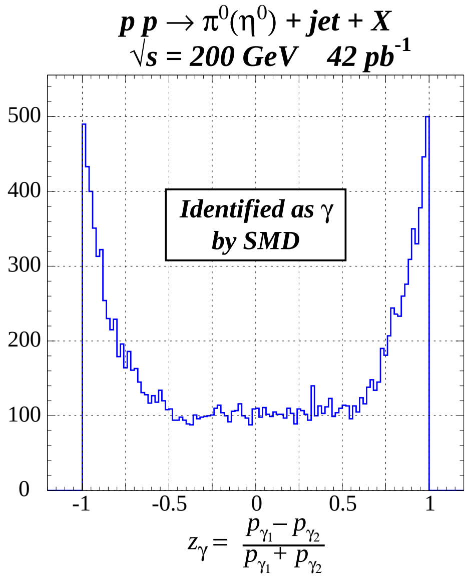

Figure A.11 Photon energy sharing distribution for $\pi^0(\eta^0)$ that pass *all* cuts (including SMD) identifying them as direct photons.

OPEN QUESTIONS

1) What is the performance comparison between a scintillator SMD and a gaseous SMD for $\pi^0(\eta^0)$ versus γ distinction?
2) How can the preshower detector be used to aid in the distinction between $\pi^0(\eta^0)$ and γ events?
3) How does $\gamma / \pi^0(\eta^0)$ discrimination vary with the depth of the SMD within the EMC stack? What is the maximum energy where this method of $\gamma / \pi^0(\eta^0)$ discrimination works?

A.4 Event Reconstruction

A.4.1 Jet Reconstruction

Jet reconstruction is based on the UA1 jet finder, suitably modified for STAR. Details of the algorithm have been discussed in an earlier STAR Note [45]. That same algorithm has been employed here. The input to the jet finder is a table of transverse energy, E_T, binned in η and ϕ. Table entries are made for all particles that fall within the acceptance of the BEMC ($|\eta| < 0.98$) or EEMC ($1.05 < \eta < 2.0$). For photons, the η,ϕ bin chosen corresponds to the tower structure of the BEMC and EEMC. For charged particles, the transverse energy at the interaction point is computed for the charged particle from the measured p_T from the TPC tracking and the charged pion mass (*i.e.*, assuming there is no particle identification available from STAR). The η,ϕ bin chosen for the charged particle results from the direction of the TPC track at the point of origin of the track. In a more proper treatment, the TPC track should be extended back to the interaction point, as is likely to be assumed in the TPC track reconstructions. Long-lived neutral hadrons (neutrons, anti-neutrons and K_L^0) are assumed to be invisible, since their interaction probability in the EMC is small.

Also input to the jet finder is the jet radius

$$R_{jet} = \sqrt{\Delta\eta^2 + \Delta\phi^2} = 0.7, \qquad \text{(A.13)}$$

where $\Delta\eta(\phi)$ refers to the difference in the direction of the observed particle from the reconstructed jet direction. A second input parameter is the jet energy threshold, set at $\Sigma E_T = 5$ GeV, the same value used in previous studies of jet reconstruction in $p + A$ and $A + A$ collisions at STAR [45].

There are several potential sources of systematic error introduced by this procedure. First, the assumption that all detected particles originate from the interaction point is incorrect for strange particles (Λ and K_S^0) that subsequently decay within the detector volume, since their decay vertex can be substantially displaced from the interaction point. It's even possible that a sizable fraction of the charged particles from Λ and K_S^0 decay would be lost in the TPC pile-up suppression procedure, since most algorithms that have been discussed reject tracks that do not point back to the interaction point. Loss of the track is likely a more serious error than incorrectly assigning its origin to the interaction point. This error has not yet been quantitatively assessed, but is expected to be small since the strangeness content of u,d quark jets is not significant. A second source of error is the assumption that all charged particles are pions. This assumption underestimates the transverse energy for $K^\pm$ and proton tracks. Preliminary studies have indicated that only very small corrections to the reconstructed jet parameters result from this assumption.

The accuracy of the jet finder results can be established by comparing the jet parameters (η_{jet}, ϕ_{jet} and $p_{T,jet}$) to those of the parton (η_{parton}, ϕ_{parton} and $p_{T,parton}$) in the final state following the hard-scattering interaction. This information is available in the PYTHIA event record. These studies are best conducted for *pp* interactions resulting in direct photon production, since typically there is only a single jet following the hard scattering. Additional jets are produced for some events from initial- (IS) and final-state (FS) QCD radiation. In general, these jets are expected to have smaller p_T compared to jets produced by recoiling quarks following gluon Compton scattering; the results presented below are for the highest p_T jet found. A more careful study of the effect of jets from IS and FS radiation on the kinematics reconstruction (discussed in the following section) is required.

In the interval, $-0.3 \leq \eta_{parton} \leq 1.3$, within a full jet radius, R_{jet}, from the edge of the EMC acceptance, the jet finder accurately reconstructs the direction of the recoiling parton (see Fig.

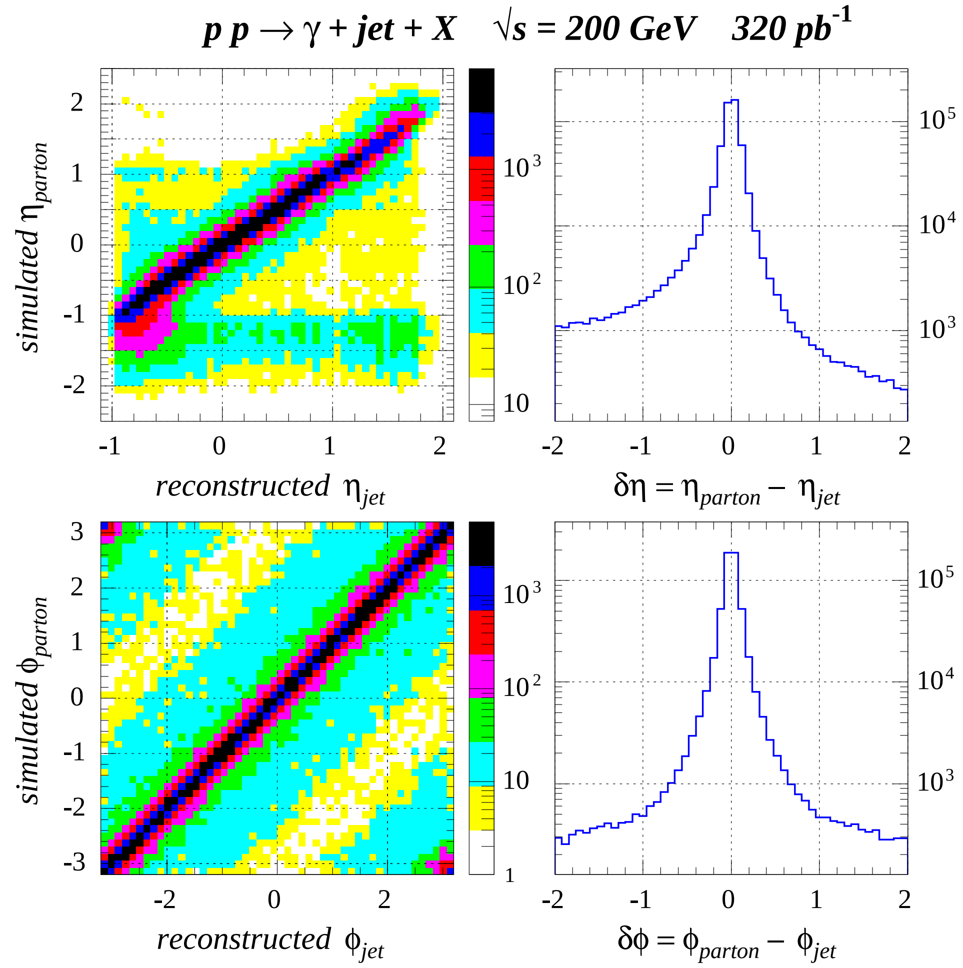

Figure A.12 Results from the UA1 jet finder for detected photons and charged particles. The events are selected by requiring a photon with $10 < p_T < 20$ GeV/c satisfying the UA2 isolation cuts. The accuracy of the jet finder results is determined from comparing the direction of the recoiling parton following a hard QCD process producing direct photons to the reconstructed jet direction. In all cases, the comparison is made to the highest p_T jet. When the recoiling parton is beyond the acceptance of the EMC (*e.g.*, at $\eta < -1$), the highest-p_T jet is often uncorrelated with the generated parton.

A.12). For final state partons in this interval, the jet finding efficiency is ~90% and the $\eta_{parton} - \eta_{jet}$ distribution is reasonably well characterized by a Gaussian distribution with $\sigma = 0.095$. There are small (~6% of all events) non-Gaussian tails to this distribution which could reflect jet reconstruction inefficiencies. Similarly, by limiting the final state parton to be within the detector acceptance, the $\phi_{parton} - \phi_{jet}$ distribution is also well described by a Gaussian with $\sigma = 0.08$ radians. The features of the ϕ_{parton} versus ϕ_{jet} correlation are consistent with the azimuthal symmetry of the STAR detector. The contributions near $|\phi_{parton}| = -|\phi_{jet}|$ in Fig. A.12 arise because ϕ is a continuous variable. In the η_{parton} versus η_{jet} correlation, it is evident that, as the final-state parton heads in directions near the edge of the acceptance of the STAR detector, the jet reconstruction resolution considerably worsens. This is especially noticeable near $\eta = -1$; the broadening of the correlation indicates loss of resolution while the intense band for $\eta < -1$ indicates that the highest p_T jet found is no longer correlated with the final-state parton from the QCD hard scattering. A similar, but fainter, band appears near the acceptance crack between the BEMC and the EEMC. These effects could be lessened by extending the η bins to include charged particles reconstructed by the TPC in the interval $-1.8 < \eta < -1$.

Examination of the accuracy of the jet energy reconstruction following a similar procedure paints a considerably different picture. Even though the correlation between $p_{T,parton}$ and $p_{T,jet}$ is clearly evident in Fig. A.13, the resolution in reconstructing the parton's energy is considerably worse than in reconstructing its direction. Also noticeable in the momentum difference spectrum is a shift of the distribution away from $\delta p_T / p_T = 0$ (where $\delta p_T = p_{T,parton} - p_{T,jet}$,) arising because of the unmeasured neutral hadron (neutrons, antineutrons and K_L^0) component of the jets. This also causes the distribution to be skewed towards positive $\delta p_T / p_T$ for events where a more significant fraction of the jet energy is carried by the undetected neutrals. Even with the inclusion of the neutral hadrons, the full-width at half maximum (FWHM) of the $\delta p_T / p_T$ distribution is still ~30%, limited by the physics of the hadronization process. In the LUND string model, used by PYTHIA for this process, momentum is shared between the recoiling parton following the hard

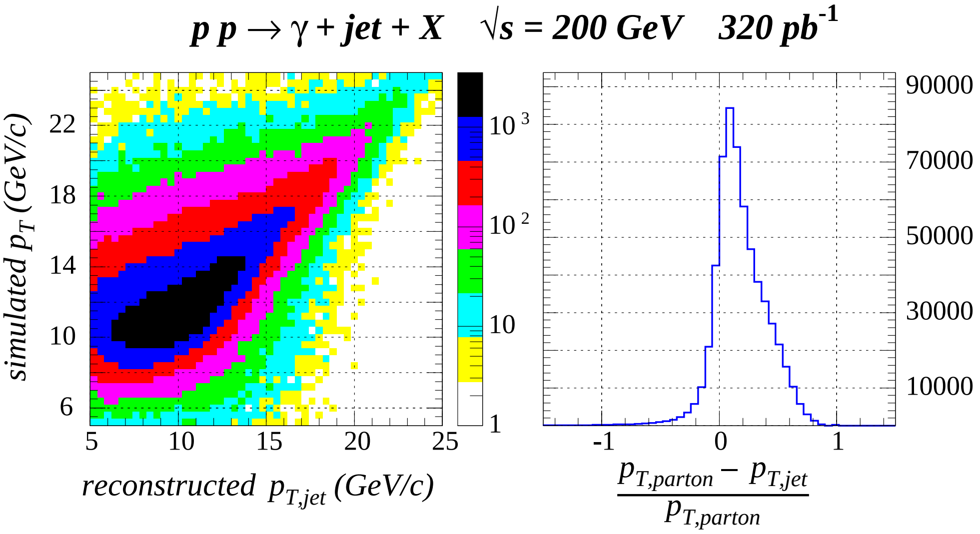
$p\,p \rightarrow \gamma + jet + X \quad \sqrt{s} = 200$ GeV $\quad 320\ pb^{-1}$

Figure A.13 Results from the UA2 jet finder for detected photons and charged particles. The same event selection criteria used for Fig. A.12 are applied. The accuracy of the jet finder results is determined from comparing p_T for the recoiling parton following a QCD process producing direct photons to the reconstructed jet p_T. In all cases, the comparison is made to the highest p_T jet.

scattering, and other partons attached to it via color fields. Hence, the dynamics of hadronization is the ultimate limitation to the determination of the energy of the recoiling parton. Because of this poor resolution, there is little to be gained in background suppression for direct photon events by requiring that p_T of the away-side jet matches p_T of the detected photon.

The jet reconstruction results presented in Figs. A.12-13 account for only the finite acceptance, but not the finite detection resolution, of the charged particles and photons that are passed to the UA1 jet finder. Finite momentum resolution effects have been included in separate studies, assuming

$$\begin{aligned} \frac{\delta E_\gamma}{E_\gamma} &= 2\% + \frac{14\%}{\sqrt{E_\gamma}}, \text{ for photons, and} \\ \frac{\delta p_T}{p_T} &= 0.011 + 0.0024 p_T, \text{ for charged particles.} \end{aligned} \qquad \text{(A.14)}$$

Inclusion of these detection resolutions results in the increase of the FWHM of the $\delta\eta$ distribution from 0.15, corresponding to the value for perfect momentum resolution for the detected particles, to 0.16, when momentum resolutions given by Eqn. A.14 are included. When accounting for finite momentum resolution of the detected particles, the resolution in the reconstruction of the p_T of the parton worsens by ~30%. As already stated, the ability to reconstruct the p_T of the parton is not central to the partonic kinematics reconstruction for γ + jet coincidence studies.

OPEN QUESTIONS

1) Can ϕ correlations between the direct photon candidate and the jet enable a suppression of the background from jets uncorrelated with the recoiling parton?
2) Is it possible to extend jet coverage closer to the edge of the STAR acceptance after inclusion of correlations with the direct photon?
3) What influence is there on jet reconstruction if charged particles from long-lived strange particles (Λ, Σ and K_S^0) would be lost due to TPC pileup rejection?

A.4.2 Partonic Kinematics Reconstruction

In principle, the full kinematics of the dominant hard scattering process that contributes to the $pp \rightarrow \gamma$ + jet + X reaction can be reconstructed from event-by-event measurements of the directions and transverse momenta of the direct photon and the away-side jet. In practice, the jet p_T resolution limits the determination of the transverse momentum of the partons in the initial state. Nonetheless, by assuming that these transverse momentum components are negligible (assuming a collinear collision), the kinematics can still be reconstructed, albeit with some remaining ambiguities, as discussed below for the $pp \rightarrow \gamma$ + jet + X reaction. The same procedure could also be applied for coincident di-jet events produced in pp collisions, but the limited p_T resolution of the jet would be a much greater liability than for γ + jet coincidences, and would prove to be the dominant source of uncertainty in the kinematic reconstructions.

Event-by-event measurements are made of the photon pseudorapidity, η_γ, and momentum p_γ. The transverse momentum in the hard scattering is reconstructed from these quantities as $p_T = p_\gamma/\cosh\eta_\gamma$. The jet pseudorapidity, η_{jet}, can then be used to write

$$
\begin{aligned}
\eta_{boost} &= \tfrac{1}{2}(\eta_\gamma + \eta_{jet}) \qquad \eta^* = \pm\tfrac{1}{2}(\eta_\gamma - \eta_{jet}) \\
\tau &= \frac{4p_T^2}{s}\cosh^2\eta^* = (x_T\cosh\eta^*)^2 \\
x_1 &= \sqrt{\tau}e^{+\eta_{boost}} = \frac{x_T}{2}\left(e^{+\eta_\gamma} + e^{+\eta_{jet}}\right) \\
x_2 &= \sqrt{\tau}e^{-\eta_{boost}} = \frac{x_T}{2}\left(e^{-\eta_\gamma} + e^{-\eta_{jet}}\right).
\end{aligned}
\tag{A.15}
$$

The remaining ambiguity is the association of x_1,x_2 with the quark and gluon momentum fractions. The general procedure is to associate the larger of the two x_1,x_2 values with the quark momentum fraction and the smaller of the two with the gluon momentum fraction.

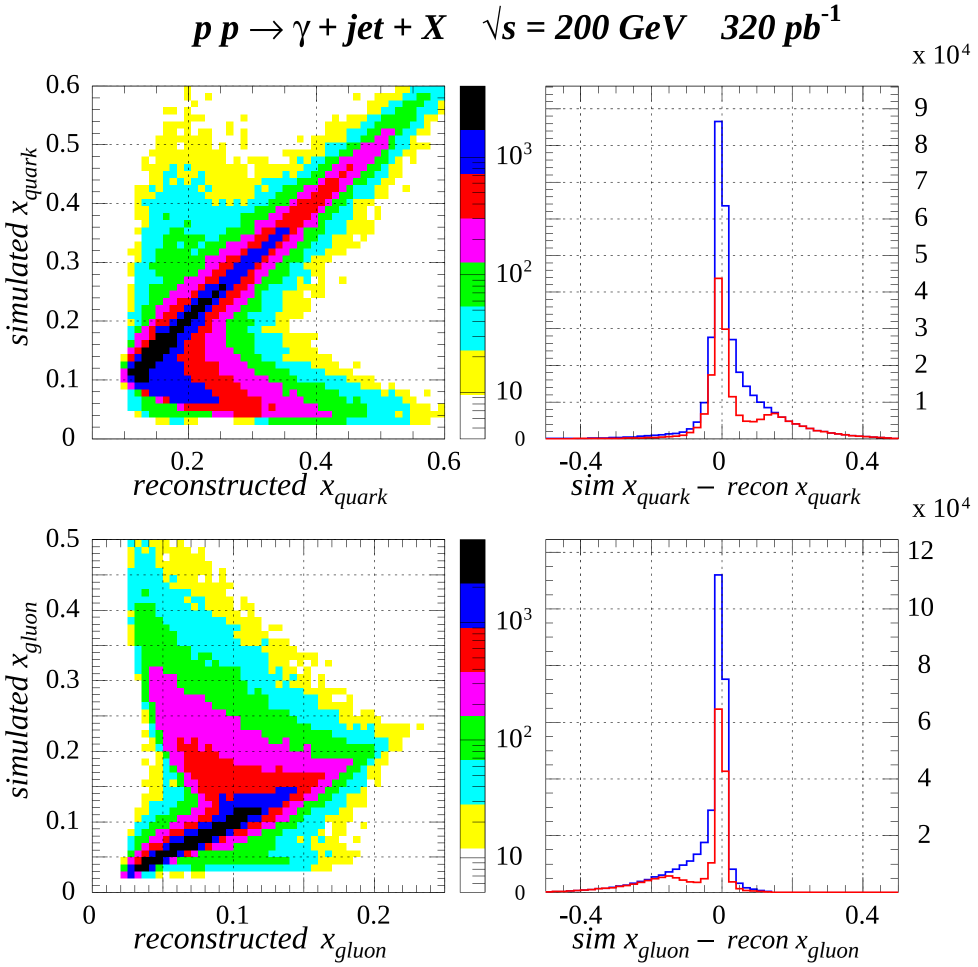

Figure A.14 Comparison of the simulated initial-state parton kinematics to reconstructed values based on measurements of η_γ, η_{jet} and $p_{T,\gamma}$ assuming collinear collisions. The simulations included initial-state radiation which introduces sizable transverse momentum components to the initial-state partons (‘k_T smearing’) not accounted for in the reconstruction. k_T smearing effects limit the resolution in the kinematic reconstruction. Perfect resolution is assumed in detecting the jet particles and the direct photon. The influence of finite detector resolution is discussed in the text. All kinematic cuts (Eqn. A.16) are included except max$\{x_1,x_2\}$ > 0.2; the light (red) line in the right-hand column includes that cut as well.

To check the effectiveness of this assumption, the quark and gluon momentum fraction used by PYTHIA in the QCD hard scattering process have been compared to the quantities defined above, reconstructed from the event sample. The cuts employed on the event sample are

$$\begin{aligned} &\text{cut 1:} \quad (10 \le p_{T,\gamma} \le 20 \text{ GeV / c}) \cdot (\text{-}1 \le \eta_\gamma \le 2) \\ &\text{cut 2:} \quad \text{UA2 `isolation cut'} \\ &\text{cut 3:} \quad (N_{jet} \ge 1) \cdot (\text{-}0.3 \le \eta_{jet} \le 1.3) \\ &\text{cut 4:} \quad \max\{x_1, x_2\} \ge 0.2 \ . \end{aligned} \qquad (A.16)$$

The results for the reconstruction of the initial-state partonic kinematics are shown in Fig. A.14. The dominant feature of the δx (defined as the difference between the simulated x and reconstructed x for the quark and gluon, respectively) distribution is the appearance of a narrow spike near zero and a broad tail to positive values for the quark and to negative values for the gluon. The tails to the distributions result from the misassignment of x_1,x_2 to the initial-state quark and gluon. These events arise when the quark momentum fraction is smaller than the gluon's in the simulated hard-scattering process. When examined on a different scale, it is clear that the gluon momentum fraction is reconstructed with a greater resolution than for the quark. This occurs because the detector asymmetry (a single end cap) favors events with positive η_{boost}, resulting in better resolution for the parton with min{x_1,x_2} by the factor $e^{2\eta_{boost}}$. It is also the case that the resolution in determining the partonic kinematics is limited by initial-state transverse momentum (k_T smearing), assumed to be absent in the reconstruction.

The results in Fig. A.14 are calculated assuming perfect resolution in determine $p_{T,\gamma}$ and η_γ. For the latter, the measured position from the SMD should result in only very small errors in determining η_γ. The influence of finite energy resolution on the direct photon (as given by Eqn. A.14) does not qualitatively change the δx_{gluon} or δx_{quark} distributions. Quantitatively, finite resolution causes the FWHM of the peak at $\delta x = 0$ to increase from 0.013(0.035) to 0.014(0.053) for gluons(quarks). Hence, the primary limitation to the reconstruction of the partonic Bjorken x value is from k_T smearing.

Of equal importance to the determination of $\Delta G(x)$ directly from the measured longitudinal spin correlation parameter, A_{LL}, is the reconstruction of the pCM scattering angle ϑ^*. This kinematic variable is essential because of the strong variation of $\hat{a}_{LL}$ with cos ϑ^*. Again, assuming collinear partonic collisions, it can be shown that

$$\cos\vartheta^* = \tanh(\pm\eta^*) . \qquad (A.17)$$

Hence, although the magnitude of cos ϑ^* is well measured, the *sign* of cos ϑ^* is not well determined for all events, as is clearly indicated in Fig. A.15. The ambiguities are minimized for photons detected in the EEMC.

Observed in Fig. A.15 is a peak atop a broad background. The background primarily arises from a sign error in the reconstruction of cos ϑ^*, and corresponds to improperly associating the quark (gluon) to the proton beam headed in the direction of the end cap. This is not identically the same error as improperly associating x_1 and x_2 with x_{quark} and x_{gluon}, although it is related when cos ϑ^* is large in magnitude. Even if the reconstructed momentum fractions are properly assigned to the quark and the gluon, it is possible to improperly associate the initial-state partons with the appropriate proton beams when $x_1 \sim x_2$. The accuracy of the reconstruction of cos ϑ^* in cases where the sign is properly determined is limited by the determination of the jet direction and by k_T smearing, with the latter being the dominant source of uncertainty. It is assumed that η_γ can be very accurately determined from the SMD position information.

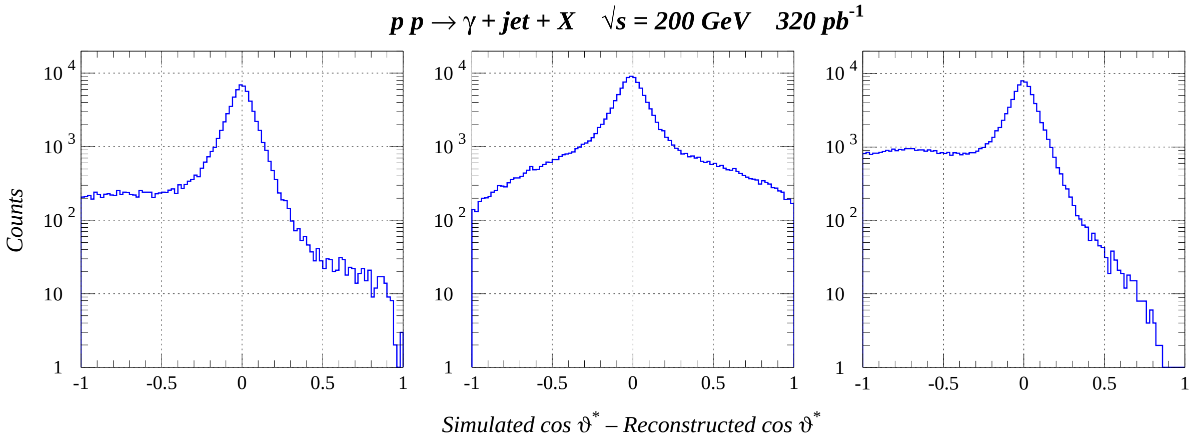

Figure A.15 Comparison of the simulated value of cos ϑ^*, the pCM scattering angle, to the reconstructed value. The differences are shown as a function of η_γ (Left) $1 \le \eta_\gamma \le 2$ (EEMC), (Middle) $0 \le \eta_\gamma \le 1$ and (Right) $-1 \le \eta_\gamma \le 0$. The 'background' arises from improper reconstruction of the sign of cos ϑ^* and is smallest in the EEMC.

A.4.3 Predictions for A_{LL} and Direct Determination of ΔG(x)

A prediction for the longitudinal spin-correlation parameter can be extracted from the simulations described above via the standard analysis

$$A_{LL} = \frac{1}{P_{b1}P_{b2}} \frac{N_{++} - N_{+-}}{N_{++} + N_{+-}}, \qquad \text{(A.18)}$$

where $N_{++(+-)}$ is the yield measured when both beams have the same (opposite) helicities. The events have been selected using all four of the cuts described in Eqn. A.16. In the simulations, the beam polarizations are assumed to be equal and are $P_{b1} = P_{b2} = 0.7$. The predicted spin correlation is given in Fig. A.16 for the Gehrmann-Stirling (GS) set A polarized parton distributions [6] approximately evolved to the appropriate scale (assumed to be $Q^2 = p_T^2 / 2$) following the procedure of Ref. [11]. The result is plotted as a function of the reconstructed gluon momentum fraction, including all of the systematic errors discussed in the previous section. The nearly linear rise of A_{LL} with x_{gluon} primarily reflects the x dependence of the gluon polarization for the particular choice of structure functions.

The polarized gluon distribution, $\Delta G(x)$, can be directly deduced from the event data, based on the leading order pQCD expression for $\hat{a}_{LL}$ for gluon Compton scattering, ignoring the contributions of $q\bar{q} \to g\gamma$, and assuming an approximate treatment of evolution. This is accomplished by using the partonic kinematics, deduced by assuming collinear partonic collisions in the initial state, to evaluate for each event: (1) the pQCD expression for the partonic spin-correlation parameter for gluon Compton scattering, *alone*, at the deduced value of cos ϑ^* for the event; (2) the 'scale' used for evolving the structure functions from the measured p_T of the direct photon, ignoring any effects of k_T smearing; (3) a parameterization of the A_1 structure function for the proton, fit to the polarized deep inelastic scattering measurements, evaluated at the deduced

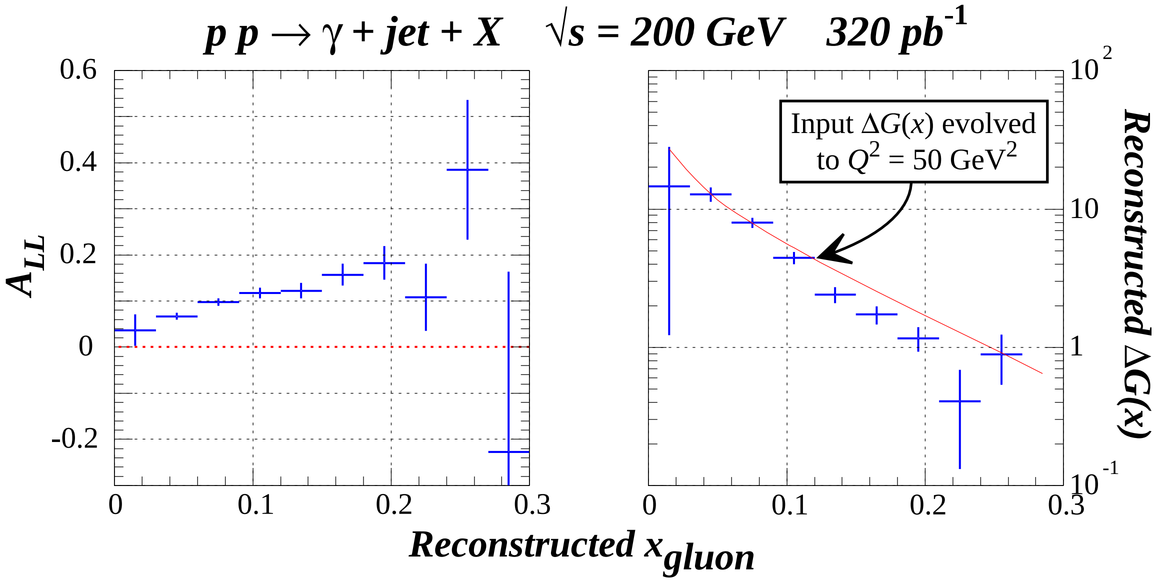

Figure A.16 (Left) The predicted value for A_{LL} using GS set A polarized structure functions [6] shown as a function of the reconstructed x_{gluon}. The errors shown are statistical only and do not reflect the contribution from subtraction of the direct meson background. (Right) Comparison of the input polarized gluon structure function to values deduced directly from the simulated data, as a function of the reconstructed x_{gluon}.

value of x_{quark} evolved to the appropriate Q^2 for the event; and (4) a parameterization of the unpolarized gluon structure function, evaluated at the deduced value of x_{gluon} and evolved to the appropriate Q^2,

$$\Delta G(x_g) = \frac{N_{++}(x_g) - N_{+-}(x_g)}{P_{b_1} P_{b_2} \sum_{i=1}^{N_{++}+N_{+-}} A_{1p}(x_{q_i}, Q_i^2)\hat{a}_{LL}(\cos\vartheta_i^*) / G(x_{g_i}, Q_i^2)}. \qquad \text{(A.19)}$$

This expression is compared to the polarized gluon structure function Gehrmann-Stirling (GS) set A input [6] to the simulation in Fig. A.16, evolved to Q^2 = 50 GeV^2 following the approximate procedure of Ref. [11]. The systematic differences between the input polarized gluon distribution and the 'reconstructed $\Delta G(x)$' arise from several sources, including

- ignoring the contribution of the $q\bar{q} \rightarrow g\gamma$ process, representing ~10% of the total yield of direct photons, which has $\hat{a}_{LL} = -1$ for all cos ϑ^*. This approximation results in an underestimate of the extracted $\Delta G(x)$.
- misassignment of the reconstructed momentum fractions to the quark and the gluon. From Fig. A.14 it is clear that most of these misassignments occur for $x_{quark} < 0.15$ and $x_{gluon} > 0.15$. One effect of this is to incorrectly associate a larger quark polarization than was actually involved in generating the event, thereby resulting in a smaller value of $\Delta G(x)$ deduced for those events. A second effect, is that the unpolarized $G(x)$ is deduced to be too large compared to the event generation. The net effect for events with misassigned x values is a reconstructed $\Delta G(x)$ distribution systematically smaller than the input GS set A, with the resulting values distributed over a range of x_{gluon}.

- finite resolution and sign misassignments in the reconstruction of cos ϑ^*. The former affects the reconstruction of $\Delta G(x)$ because $\hat{a}_{LL}$ is a non-linear function of cos ϑ^* for gluon Compton scattering. The latter enter because the $\hat{a}_{LL}$ used to generate the event is not the same as that used to reconstruct the event.
- initial-state radiation, or k_T smearing effects. These effects introduce non-zero transverse momentum in the initial state contrary to the assumption of collinear collisions. The end result is to make correlated errors in the reconstruction of x_{quark} and x_{gluon}. It is possible that for events with sufficiently large k_T smearing, a second jet can be reconstructed and the collinear approximation to the kinematic reconstruction can be relaxed.

Even with these errors introduced by the simplifying assumptions used in the event reconstructions, the reconstructed $\Delta G(x)$ deviates by at most 30% from the input distribution, mostly at large x_{gluon} values where the assignments of the reconstructed momentum fractions to the quark or the gluon are most prone to error. Those deviations will be somewhat larger when all points of the $\Delta G(x)$ distribution are evolved to a common Q^2, a necessary step since there is a strong correlation between the reconstructed x_{gluon} and $p_{T,\gamma}$. Since the errors associated with the direct extraction of $\Delta G(x)$ from the simulated spin asymmetry measurements appear to be small, Monte-Carlo simulations should be adequate to apply corrections to the extracted values.

A major concern about the A_{LL} measurements for the $\vec{p}\vec{p} \to \gamma + \text{jet} + X$ reaction is the magnitude of *systematic*, rather than statistical, errors in the measured spin asymmetries. There are potentially sources of *false asymmetry* that could ultimately limit the accuracy of the A_{LL} measurements, and hence the accuracy of the reconstructed $\Delta G(x)$. We have examined how such false asymmetries would influence both the A_{LL} measurement and the reconstruction of $\Delta G(x)$. The method used was to assume some source of false asymmetry of unknown origin that varied event by event. We chose to modify the spin-dependent asymmetry, $\varepsilon = P_{b_1} P_{b_2} A_{LL}$, used in Eqn. A.7 by an amount $\delta\varepsilon$, chosen at random for each event from a Gaussian distribution of mean equal to 0.005 and $\sigma = 0.005$. The introduction of a *false asymmetry* of this sort causes a small increase in A_{LL} for each bin, and correspondingly, the reconstructed $\Delta G(x)$. The results shown in Fig. A.16 have $\delta\varepsilon = 0$ for all events. As well, the results shown in Fig. A.16 do not include finite resolution effects in the detection of the direct photon. These effects will be discussed below (Sec. A.4.5).

As discussed below (see Sec. A.4.5), it is essential to perform good measurements of the $\vec{p}\vec{p} \to \gamma + \text{jet} + X$ reaction at *both* $\sqrt{s} = 200$ and 500 GeV, to minimize the extrapolation errors (in the limit, $x_{gluon} \to 0$) in determining the zeroth moment of $\Delta G(x)$, defined in Eqn. A.1. To assess what is the expected magnitude of A_{LL} and what is the efficacy of the *direct extraction* of $\Delta G(x)$ from measured spin-dependent asymmetries at $\sqrt{s} = 500$ GeV, comparable calculations for the $\vec{p}\vec{p} \to \gamma + \text{jet} + X$ reaction at this higher energy have been performed. The results for the spin correlation coefficient and for the direction reconstruction of $\Delta G(x)$ are shown in Fig. A.17.

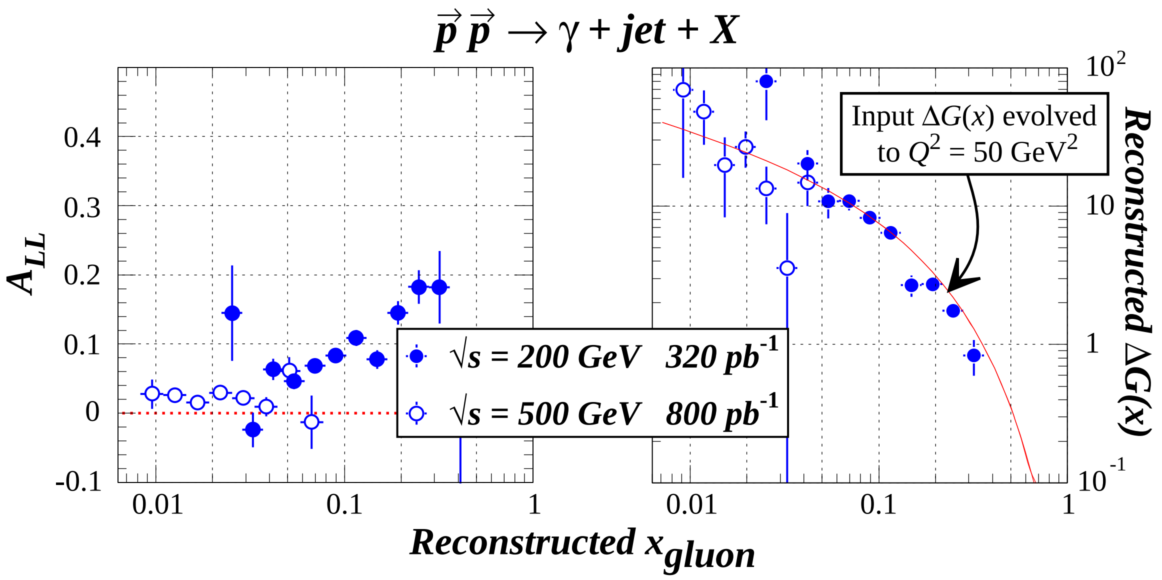

Figure A.17 (Left) The predicted value for A_{LL} using GS set A polarized structure functions [6] shown as a function of the reconstructed x_{gluon} for $\sqrt{s}$ = 200 and 500 GeV measurements. The errors shown are statistical only and do not reflect the contribution from subtraction of the direct meson background. (Right) Comparison of the input polarized gluon structure function to values deduced directly from the simulated data, as a function of the reconstructed x_{gluon}.

The following observations and comments about Fig. A.17 can be made:

- the overlap in reconstructed x_{gluon} for measurements at the two collision energies is limited by the constraint, $10 \leq p_{T,\gamma} \leq 20$ GeV/c. This constraint is necessary to ensure comparable $\pi^0(\eta^0)$ background suppression at the two collision energies. Although the background:signal ratio for $p_T \geq 20$ GeV/c is expected to decrease exponentially (Figs. A.6,8), the ability to directly measure the neutral meson background from the response of the SMD diminishes, since the opening angle between the two decay photons decreases inversely with increasing meson energy.
- the values for A_{LL} at $\sqrt{s}$ = 500 GeV, for this model of $\Delta G(x)$ input to the calculations, are predicted to be quite small, relative to the values at $\sqrt{s}$ = 200 GeV. This, along with problems associated with the increased pileup in the TPC at the higher collision energy, suggests that a thorough understanding of systematic errors at the lower collision energy is essential before embarking on the higher energy measurements.
- the systematic errors in the *direct extraction* of $\Delta G(x)$ from the measured asymmetries show similar trends at the two collision energies. For fixed $\sqrt{s}$, the deviations from the input value of $\Delta G(x)$ have a monotonic dependence on x_T (as defined in Eqn. A.15), and hence on the reconstructed x_{gluon}. The departure from the input structure function is greatest at large x_T, suggesting that k_T smearing effects play the most important role in the deviation between the extracted and input values of $\Delta G(x)$, albeit with comparable magnitude effects at the two energies.

The principal conclusion that can be drawn from Fig. A.17 is that $\sqrt{s}$ = 500 GeV direct photon + jet measurements will provide an essential extension of the x_{gluon} range, without introducing substantially greater systematic errors in directly relating the spin asymmetry measurements to the polarized gluon structure function.

OPEN QUESTIONS

1) To what extent can more sophisticated algorithms eliminate the misassignments of the reconstructed momentum fractions to the initial-state quark and gluon?
2) What is the minimum initial state k_T that would allow a reliable reconstruction of a second final-state jet?

A.4.4 Background Contributions

The kinematic cuts (specified in Sec. A.4.2) used to identify valid γ + jet coincidences influence the $\pi^0(\eta^0)$ background and select out portions of the phase space for direct photon events. Their influence for $\sqrt{s}$ = 200 GeV *pp* collisions is shown in Fig. A.18. The single cut most responsible for shaping the η distributions of both direct meson and direct photon events is the $\max\{x_1, x_2\} > 0.2$ condition, employed to ensure large polarization for the struck quark in gluon Compton scattering. This cut selects events away from mid-rapidity, in the direction of the EEMC. The p_T distributions are cut off by the condition $10 \le p_T \le 20$ GeV/c. The other conditions cause a slight steepening of the slope of the background:signal ratio versus p_T. The influence of the SMD cuts for distinguishing photons from direct mesons, based on the algorithm discussed in Sec. A.3.2, is shown in Fig. 15. The pseudodetector, described in Sec. A.2.3, is used to simulate the response of both the BEMC and the EEMC. It is likely that the $\pi^0(\eta^0)$ background suppression is better in this simulation than will be observed in the actual measurements, particularly for $|\eta| < 1$, because the peak-fitting analysis of the SMD is based on the response of triangular cross section scintillator detectors, rather than the gaseous SMD that is being built for the BEMC. On the other hand, the overestimate of the suppression factor may not be too severe, since the energies of the $\pi^0(\eta^0)$ at mid-rapidity are smaller than in the endcap region for the same p_T.

As discussed in Sec. 3.3, the direct photon spin correlation, A_{LL}, must be determined from the event samples that *pass* and those that *fail* the SMD identification as direct photon candidates. Of particular importance is the spin correlation for the $\pi^0(\eta^0)$ background events identified as direct photons, shown in Fig. A.19 at $\sqrt{s}$ = 200 GeV. (Analogous background simulations for $\sqrt{s}$ = 500 GeV are extremely time consuming, and have not yet been completed.) Significant values can result since direct mesons arise primarily from *gg* and *qg* elastic scattering processes, each of which has a sizable partonic $\hat{a}_{LL}$. The magnitude of the background subtraction error (as discussed in Sec. 3.3) depends on the differences between A_{LL} for the photon production signal and the meson production background. Comparison of Figs. A.16 and A.19 suggests that the magnitude of this difference varies from 0 to 0.3 as a function of the reconstructed x_{gluon}.

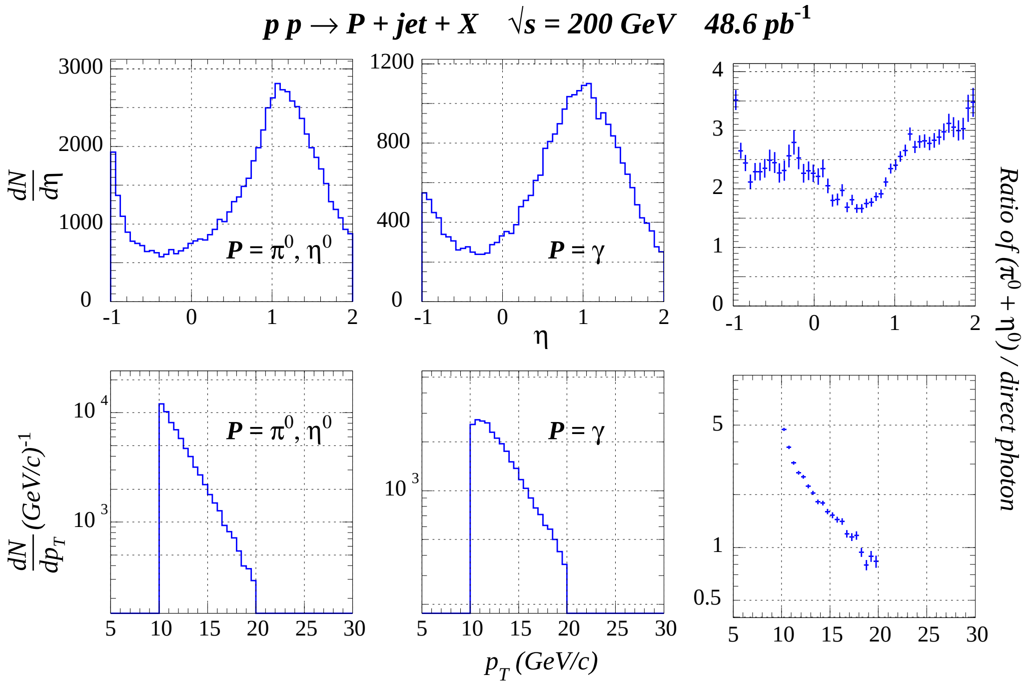

Figure A.18 Direct meson (π^0,η^0) and direct photon yields from PYTHIA versus pseudorapidity (top) and versus p_T (bottom) for pp collisions at $\sqrt{s}$ = 200 GeV. The rightmost column of the figure shows the ratio. All kinematic conditions (excluding the SMD) are used to select events, as specified in Sec. A.4.2. The results here differ from those in Fig. A.8 primarily due to the influence of an additional cut requiring $\max\{x_1,x_2\} \geq 0.2$.

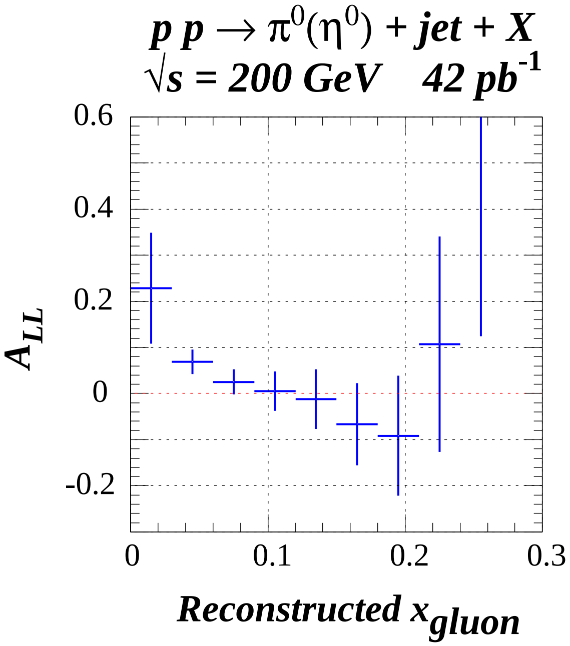

Figure A.19 Spin correlation coefficient for meson (π^0,η^0) background to direct photon production in longitudinally polarized proton collisions at $\sqrt{s}$ = 200 GeV. All kinematic conditions, as specified in Eqn. A.16, and cuts on the SMD are used to select events. This event sample passes all of the SMD cuts for *direct photons*.

A.4.5 Determination of Integral ΔG and EMC Calibrations

A good determination of the zeroth moment of $\Delta G(x)$, defined in Eqn. A.1, requires not only the ability to determine the x_{gluon} dependence of the polarized gluon structure function, but also an assessment of the magnitude of the extrapolation errors in going from the experimentally measured x_{gluon} range to the full interval, $0 \le x_{gluon} \le 1$. This assessment is addressed here by fitting *uncorrected* values for $\Delta G(x)$, directly extracted from simulations of the spin asymmetry measured for the $\vec{p}\vec{p} \to \gamma + \text{jet} + X$ reaction, to a functional form used previously in parameterizations of both polarized and unpolarized structure functions.

Eqn. A.20 represents one method [6] of parameterizing the x-dependence of the polarized gluon structure function:

$$x\Delta G(x) = \eta_G A x^{a_G}(1-x)^{b_G}(1+\rho_G x^{1/2} + \gamma_G x). \qquad \text{(A.20)}$$

Ideally, a sufficient range of x_{gluon} would be covered in measurements to enable a five-parameter fit to the polarized gluon structure function to determine (1) the normalization η_G; (2) the exponents a_G and b_G, describing respectively the small- and large-x_{gluon} variation of the structure function; and (3) the coefficients ρ_G and γ_G in the power series in $\sqrt{x}$, describing the detailed shape of the structure function. The factor A in Eqn. A.20 is chosen so that the zeroth moment of $\Delta G(x)$ can be identified with η_G:

$$A^{-1} = \left(1 + \frac{\gamma_G a_G}{a_G + b_G + 1}\right)\frac{\Gamma(a_G)\Gamma(b_G+1)}{\Gamma(a_G+b_G+1)} + \rho_G \frac{\Gamma(a_G+\frac{1}{2})\Gamma(b_G+1)}{\Gamma(a_G+b_G+1)}, \qquad \text{(A.21)}$$

where $\Gamma(x)$ is the well-known gamma function. By making the integral of $\Delta G(x)$ a fitting parameter, extrapolation errors are automatically included by the correlations between η_G and the other fitting parameters.

Fits to $\Delta G(x)$ extracted from simulated values for the spin asymmetry cannot determine all five of the parameters in Eqn. A.20. In particular, the exponent specifying the large-x_{gluon} dependence of the polarized gluon structure function is fixed to $b_G = 5.71$, and the value of γ_G is fixed to be zero, values taken from Ref. [6]. The MINUIT optimizer is used to determine the other three parameters (η_G, a_G and b_G) in a fit to the $\sqrt{s} = 200$ GeV results *alone*. The simulations in Fig. A.20 differ from those shown earlier (Fig. A.16) by the inclusion of finite detector resolution effects for the direct photon. This primarily affects the statistical accuracy for $\Delta G(x)$ in the smallest x_{gluon} bin, since contributions to the yield from direct photons produced in a hard scattering with $p_{T,\gamma} < 10$ GeV/c are possible when the finite detection resolution is accounted for. The results for the fit of Eqn. A.20 to the *uncorrected* values for $\Delta G(x)$ is shown in Fig. A.20. The conclusion from this analysis is that measurements of the $\vec{p}\vec{p} \to \gamma + \text{jet} + X$ reaction at $\sqrt{s} = 200$ GeV, *alone,* are insufficient to determine the integral of $\Delta G(x)$ to the accuracy necessary to allow a meaningful assessment of the constituent quark model. The problem lies simply in the x_{gluon} range spanned by the planned measurements at a single energy. The variation in the fitted exponent a_G is simply too large to enable a more accurate determination of η_G.

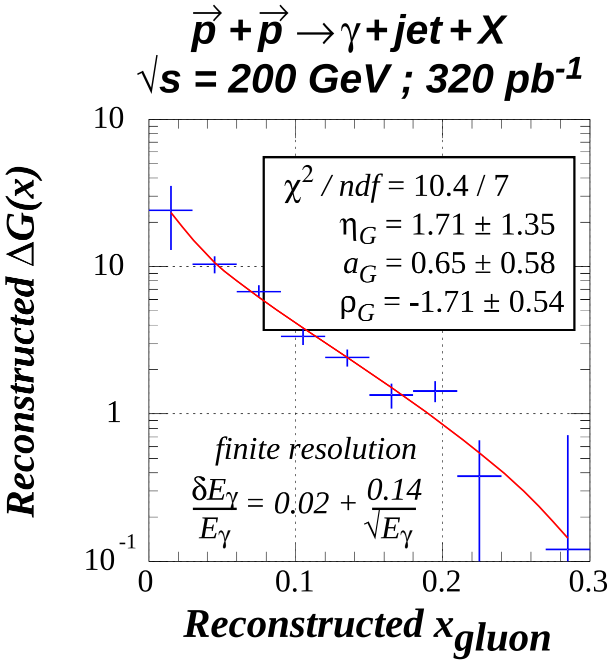

Figure A.20 The data points result from the direct extraction of $\Delta G(x)$ from simulations of the spin asymmetry for the $\vec{p}\vec{p} \rightarrow \gamma + \text{jet} + X$ reaction at $\sqrt{s}$ = 200 GeV, including finite resolution for the detected photon. The solid curve is a fit with Eqn. A.20, to assess extrapolation errors in determining the integral over all x. The integrated ΔG is equal to the fitted parameter η_G. The large uncertainty in the fitted η_G results from sizable correlations with the fitted exponent a_G, specifying the small-x_{gluon} variation of the polarized gluon structure function.

As is demonstrated in Figs. 18 and A.17, the range of x_{gluon} for which $\Delta G(x)$ is determined at STAR can be extended to the crucial small-x region by a second 10-week run at $\sqrt{s}$ = 500 GeV. The importance of these additional measurements is illustrated by fitting the *uncorrected* $x\Delta G(x)$, directly extracted from the simulated spin asymmetry measurements at $\sqrt{s}$ = 200 and 500 GeV, to the expression in Eqn. A.20. The resulting uncertainty in η_G is reduced by more than a factor of 5, reflecting the addition of points in the small-x_{gluon} range, essential to constrain the extrapolation $x_{gluon} \rightarrow 0$. The quality of the fit in Eqn. A.20 is limited because of the systematic errors in the direct extraction of $\Delta G(x)$ which vary monotonically with x_{gluon} for each collision energy. Correcting $\Delta G(x)$ will result in small shifts of the data points. Such shifts have a minimal effect on the η_G uncertainty; that quantity is primarily driven by the range of x_{gluon} spanned by the data and the magnitude of the error bars for each point. It is interesting to note that even without any corrections to $\Delta G(x)$, the extracted values of η_G and a_G are very close to those for the polarized gluon distribution input to the simulations (the Gehrmann and Stirling [6] set A parameterization of $\Delta G(x)$ has η_G = 1.71 and a_G = 0.724). This suggests that the necessary corrections will not have a large impact on the integral ΔG.

A second thing to note from Fig. A.21 is the magnitude of the errors for $x\Delta G(x)$. In the smallest x_{gluon} bins, the statistical uncertainties for the $x\Delta G(x)$ values directly extracted from the simulated spin asymmetries are quite large, even though the corresponding uncertainties for A_{LL} are very small (as shown in Fig. A.17). This is caused by the rapid growth of the unpolarized gluon structure function, $G(x)$, as x_{gluon} decreases (see Fig. A.2*b*). The net result is to make the denominator in Eqn. A.19 very small.

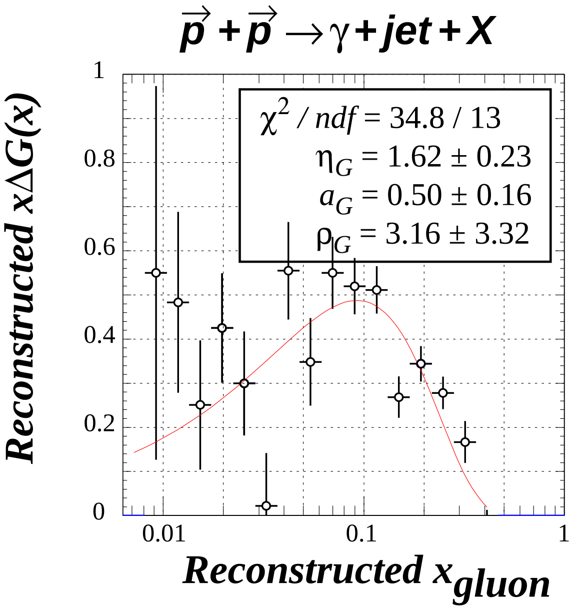

Figure A.21 The data points result from combining the *uncorrected* direct extraction of $x\Delta G(x)$ from simulations of the spin asymmetry for the $\vec{p}\,\vec{p} \rightarrow \gamma + \text{jet} + X$ reaction from two 10-week runs at $\sqrt{s}$ = 200 and 500 GeV. The solid curve is a fit to Eqn. A.20, to assess extrapolation errors in determining the integral over all x. The integrated ΔG is equal to the fitted parameter η_G. The uncertainty in η_G is substantially smaller than extracted from an analysis of the $\sqrt{s}$ = 200 GeV data alone (Fig. A.20) because of the points at small x_{gluon} produced from the $\sqrt{s}$ = 500 GeV data. The large χ^2 reflects the fact that no systematic error corrections have been applied to $\Delta G(x)$ for the simplifying assumptions in the data analysis.

The influence of the absolute gain calibration of the barrel and endcap EMC on the integral ΔG has been explored by introducing a ±5% gain shift in the determination of the absolute photon energy before the kinematic reconstruction and the application of the event selection criteria specified in Eqn. A.16. A miscalibration of the absolute photon energy scale affects the statistical errors in the different reconstructed x_{gluon} bins because of the exponential falloff of the direct photon yield with p_T. As well, there are correlated errors introduced in the determination of x_{quark} and x_{gluon} (see Eqn. A.15), producing systematic errors in the direct extraction of $\Delta G(x)$ from the spin asymmetries. The fits to the uncorrected $\Delta G(x)$ values extracted with this gain shift present demonstrate that the absolute gain calibration of the EMC must be known to a precision ±2% to keep the energy calibration contribution smaller than the overall systematic error desired for the measurement. The plans for calibrating the energy scale of the endcap EMC are discussed in Sec. 3.7.

A.5 Summary

Studies of the contribution that gluons make to the polarization of the proton are the next logical step in unraveling the spin structure of the nucleon. Based on the results presented above, we believe that the addition of an endcap electromagnetic calorimeter to STAR will enable the *world's best measurement* of $\Delta G(x)$, and its integral, via a of study of the $\vec{p}\,\vec{p} \rightarrow \gamma + \text{jet} + X$ reaction at $\sqrt{s}$ = 200 and 500 GeV.

Additional References

[56] *The Electromagnetic Calorimeter for the Solenoidal Tracker at RHIC, A Conceptual Design Report*, LBL PUB-5380 (1993).

[57] M. Hirai, S. Kumano and M. Miyama, Comput. Phys. Commun. **108**, 38 (1998).

[58] Mrinmoy Bhattacharjee and Arnaud Lucotte, D0-note 3398 (1998).

[59] *Review of Particle Properties*, European Phys. Journ. **3** (1998).

[60] H. Wind, Nucl. Instr. Meth. **115**, 431 (1974).

[61] Thomas J. LeCompte, STAR Note 306 (1997).

[62] A.A. Derevschikov, *et al*. STAR Note 305 (1997).